

## AGE DETERMINATIONS OF THE HYADES, PRAESEPE, AND PLEIADES VIA MESA MODELS WITH ROTATION

SETH GOSSAGE<sup>1</sup>, CHARLIE CONROY<sup>1</sup>, AARON DOTTER<sup>1</sup>, JIEUN CHOI<sup>1</sup>, PHILIP ROSENFELD<sup>1</sup>, PHILIP CARGILE<sup>1</sup>, ANDREW DOLPHIN<sup>2</sup>

*Accepted to ApJ*

### ABSTRACT

The Hyades, Praesepe, and Pleiades are well studied stellar clusters that anchor important secondary stellar age indicators. Recent studies have shown that main sequence turn off-based ages for these clusters may depend on the degree of rotation in the underlying stellar models. Rotation induces structural instabilities that can enhance the chemical mixing of a star, extending its fuel supply. In addition, rotation introduces a modulation of the star's observed magnitude and color due to the effects of gravity darkening. We aim to investigate the extent to which stellar rotation affects the age determination of star clusters. We utilize the MESA stellar evolution code to create models that cover a range of rotation rates corresponding to  $\Omega/\Omega_c = 0.0$  to  $0.6$  in  $0.1$  dex steps, allowing the assessment of variations in this dimension. The statistical analysis package, MATCH, is employed to derive ages and metallicities by fitting our MESA models to Tycho  $B_T$ ,  $V_T$  and 2MASS  $J$ ,  $K_s$  color-magnitude diagrams. We find that the derived ages are relatively insensitive to the effects of rotation. For the Hyades, Praesepe, and Pleiades, we derive ages based on synthetic populations that model a distribution of rotation rates or a fixed rate. Across each case, derived ages tend to agree roughly within errors, near 680, 590, and 110 – 160 Myr for the Hyades, Praesepe, and Pleiades, respectively. These ages are in agreement with Li depletion boundary-based ages and previous analyses that used non-rotating isochrones. Our methods do not provide a strong constraint on the metallicities of these clusters.

*Keywords:* stars: general, stars: rotation, Hertzsprung-Russell and C-M diagrams, open clusters: individual (The Hyades, The Praesepe, The Pleiades)

### 1. INTRODUCTION

Stellar populations serve as landmarks in understanding the cosmological timeline and as laboratories for testing stellar evolution theory. Star clusters are among the most powerful objects for use in calibrating stellar models owing to the common age, metallicity and distance of their member stars. The most nearby clusters are in many ways best suited for this type of work due to the high quality data ranging from deep color-magnitude diagrams (CMDs), high resolution spectroscopy, and asteroseismology. As such, so-called benchmark clusters like the Hyades, Praesepe, and Pleiades offer some of the best chances of ensuring the accuracy of our models.

Isochrone construction and usage of the Li depletion boundary (LDB) are two of the primary methods for accessing the ages of such clusters. Basri et al. (1996) were the first to successfully detect the LDB using faint stars in the Pleiades in conjunction with stellar models of Nelson et al. (1993), and derive an age estimate. Isochrones are stellar models covering a range of masses, paused at a moment in time, similar to how we often observe a collection of stars at a single moment. Hence, isochrones are an intuitive means of modeling stellar populations and have a long employment history in astronomy (e.g., Perrin et al. 1977; VandenBerg et al. 2002; Jørgensen & Lindegren 2005; Jeffery et al. 2016; Yen et al. 2018). Both of these methods are model-dependent, simulating the observables that we collect in databases. Therefore,

these methods are subject to the adopted physical assumptions, which are not universal. Nonetheless, model-dependent age determination techniques are widely applicable. Meanwhile, they also serve to test our composite theory of stellar evolution, relying on all of its underlying framework to make credible stellar analogues and predictions.

A number of empirical secondary age determination techniques count on knowing the ages of these clusters, as derived from model-dependent methods (see Soderblom et al. 2009 for a review). For instance, gyrochronology uses these ages to calibrate mass-period relations (e.g. Barnes 2007; Mamajek & Hillenbrand 2008) and offers the possibility of a high precision tool for determining ages of individual field stars. The zero-point of the relations between these quantities and age is set by the assumed ages of clusters like the Hyades, Praesepe, and Pleiades. The accuracy of gyrochronological results may be compromised if significant uncertainty exists in the ages on which its formalism is built.

Researchers have theorized how rotation may affect the behavior of stars for nearly a century (von Zeipel 1924; also see e.g., Shajn & Struve 1929 and references therein). However, large databases of stellar models that incorporate these effects have only become available within the last decade or so; e.g. STERN Brott et al. (2011), Geneva Ekström et al. (2012) (also Meynet & Maeder 1997; Maeder 1997; Maeder & Zahn 1998; Maeder 1999; Maeder & Meynet 2000a; Meynet & Maeder 2000), and recently MIST (Choi et al. 2016). These models take different approaches to modeling the complex effects of

<sup>1</sup> Harvard-Smithsonian Center for Astrophysics, 60 Garden Street, Cambridge, MA 02138, USA

<sup>2</sup> Raytheon, 1151 E. Hermans Road, Tuscon, AZ 85706, USA

rotation, however they all rely on some common theoretical principles. Rotation is thought to alter the chemical mixing within stars due to several induced hydrodynamical instabilities (see e.g. [Heger & Langer 2000](#); [Maeder & Meynet 2000b](#)). As a consequence, the core of a rotating star may gain access to a greater fuel supply than otherwise, leading to both greater luminosity and an extended lifetime. Furthermore, a rotating star may become significantly oblate due to latitudinally dependent centrifugal forces. As described by [von Zeipel \(1924\)](#), this effect, at times known as *gravity darkening*, introduces a substantial viewing angle dependence to the observed color and magnitude of a star. Combined, rotationally enhanced chemical mixing and gravity darkening are able to substantially alter the color and magnitude position of key stellar population features on a CMD, particularly the main-sequence turn off (MSTO).

Classically, non-rotating isochrones and stellar models have been used to determine the ages of these benchmark clusters (e.g. [Mermilliod 1981](#); [Mazzei & Pigatto 1988](#); [Meynet et al. 1993](#); [Perryman et al. 1998](#); [Kalirai & Tosi 2004](#)). However, recent studies have highlighted that a significant degree of uncertainty remains in how we model these systems. For instance, [Brandt & Huang \(2015a\)](#) in fitting these clusters with a coarse grid of rotating Geneva stellar models, interpolated with a finer grid of non-rotating PARSEC models ([Girardi et al. 2002](#)), discovered that the Praesepe and Hyades may be older than previously thought. The effects of rotation, in their modeling resulted in a best-fit age of  $\sim 800$  Myr, compared to the classically inferred ages of  $\sim 600$  Myr found via non-rotating models. This discrepancy motivates us to investigate the extent to which stellar rotation affects key cluster parameters, such as age and metallicity, and how extensively this uncertainty might exist across our stellar models.

The importance of rotation for interpreting open cluster CMDs extends well beyond these three benchmark clusters. Recent studies exploring the effects of rotation have been motivated by the potential for rotational effects to explain the extended main sequence turn offs (eMSTOs) of clusters residing in the Large and Small Magellanic Cloud (LMC and SMC); e.g. [Girardi et al. \(2013\)](#); [Correnti et al. \(2015\)](#). It is still an ongoing debate as to the level that stellar rotation is responsible for this phenomenon, e.g. [Bastian & de Mink \(2009\)](#); [Goudfrooij et al. \(2014\)](#); [Brandt & Huang \(2015b\)](#); [Piatti & Cole \(2017\)](#). Certainly, as demonstrated by [Maeder & Meynet \(2000b\)](#); [Heger & Langer \(2000\)](#) and others, rotation can have strong effects on stars during and near the MSTO phase. The consequent flux and temperature alterations that result from rotational effects may cause an observer to perceive a MSTO that is collectively brighter or fainter in reality, compared to its theoretically non-rotating model. A brighter or younger MSTO mimics either a younger or older stellar population respectively. Furthermore, with a distribution of stars at various rotation rates and viewing angles, there is a possibility for the appearance of an eMSTO, as now a distribution of fainter and brighter stars (i.e., due to rotation) coexist within the population.

Furthermore, rotation can affect the integrated light of stellar populations as well. The impact of stellar rotation on bolometric luminosity and the ionizing spectra of mas-

sive stellar populations was explored by e.g. [Levesque et al. \(2012\)](#); [Choi et al. \(2017\)](#). Both groups modeled the interplay between stellar rotation and the integrated light of galaxies whose spectral energy is dominated by the output from massive stars. In either case, rotation could enhance the ionizing radiation output of massive stars in quantity and duration (although to varying degrees, dependent on model assumptions). In affecting the population’s composite spectral properties, which are tied to its inferred stellar mass and star formation history (see e.g., [Conroy 2013](#) for a review), rotation may have far-reaching implications in extragalactic astronomy.

Here we present results derived from a self-consistent set of stellar evolution models, similar to the MIST models developed by [Choi et al. \(2016\)](#) (see also [Dotter 2016](#)), but with a larger range in rotation rate as well a custom mass and metallicity range. These models require neither major interpolations nor extrapolations over stellar mass or metallicity, as has been required in the past. Following an overview of the data featured in §2, this paper presents a base description of the physics underlying our models (§3.1), leaving further details to the aforementioned MIST papers. We detail the methods used in applying our models to observed data through a statistical analysis package known as MATCH, written by [Dolphin \(2002\)](#), in §3.3. Subsequently we discuss the results of applying our models to observations of the Hyades, Praesepe, and Pleiades clusters in §4, and cast the implications of our findings in a broader context in §5. Finally, our work is summarized in §6.

## 2. DATA

In this section we provide a summary of the photometric data used in our CMD fitting for the Hyades (§2.1), Praesepe (§2.2), and Pleiades (§2.3) clusters. We also provide a brief summary of the salient properties of each cluster. Although metallicities are cited, we do not adopt any of these listed values. We only use them to compare with our CMD-derived metallicities in later sections.

### 2.1. The Hyades

Of our target clusters, the Hyades is nearest to our solar system, making it a popular object of study amongst astronomers for many years (e.g., [Smart 1939](#); [Wayman 1967](#); [van Altena et al. 1997](#); [Reino et al. 2018](#)). We adopt a distance modulus  $\mu = 3.349$  mag ( $46.75 \pm 0.46$  pc) from [Gaia Collaboration et al. \(2017\)](#) and an extinction of  $A_V = 0.0031$  ([Taylor 2006](#)). Historically, the age of the cluster has been determined to be around 600 Myr, according to non-rotating isochrone fits; for example, [Perryman et al. \(1998\)](#) derive an age of  $625 \pm 50$  Myr from fitting optical CMD data. [Martín et al. \(2018\)](#) measured Li surface abundance in 6 brown dwarf candidates of the Hyades, and using the models of [Baraffe et al. \(2015\)](#), derived an age of  $650 \pm 70$  Myr. The Hyades may have a  $[\text{Fe}/\text{H}] = 0.103 \pm 0.008$  according to [Taylor & Jonev \(2005\)](#); recently, [Cummings et al. \(2017\)](#) found  $0.146 \pm 0.004$  from spectra of 37 Hyads.

Our optical data is comprised of the “high fidelity” stellar members identified by [de Bruijne et al. \(2001\)](#); these are stars with relatively high membership likelihood and evidence supporting their status as single stars. Binary systems are removed from this sample, and so our assumed binary fraction is zero. This catalogue is

**Table 1**  
Adopted Cluster Parameters

Cluster	$\mu^1$	$A_V^2$	$B_T, V_T$ Binary Fraction	$J, K_s$ Binary Fraction <sup>3</sup>
The Hyades	3.349 (Gaia Collaboration et al. 2017)	0.0031 (Taylor 2006)	0.0	0.25
The Praesepe	6.26 (Gáspár et al. 2009)	0.0837 (Taylor 2006)	0.0	0.30
The Pleiades	5.64 (Gaia Collaboration et al. 2016)	0.1054 (Taylor 2008)	0.0	0.0

<sup>1</sup> Distance modulus

<sup>2</sup> Interstellar reddening

<sup>3</sup> NIR data has not been cleaned of binaries for the Hyades/Praesepe.

based on the main Hipparcos catalogue (Perryman et al. 1997), utilizing derivations of secular parallaxes for cluster candidates to determine membership likelihoods. Using these high fidelity members, we fit stars with  $V_T < 8$  magnitudes, forcing the fitting algorithm to focus on the age-sensitive MSTO.

Due to the close proximity of the Hyades a significant spread in the apparent magnitudes will exist due to differential distance effects. This effect must be accounted for when fitting observed CMDs of the Hyades to models. de Bruijne et al. (2001) manage this by considering the absolute magnitude of stars (in their case derived using e.g. the Hipparcos secular parallaxes from the main catalogue, and recorded in their data tables). We do the same, but convert back to an apparent magnitude using the average distance modulus,  $\mu$ , of the Hyades cluster,  $\mu = 3.349$  mag. In essence, we place all stars at the mean distance of the cluster.

Our infrared data is sourced by the members of Goldman et al. (2013), who used the members of Röser et al. (2011), where the former researchers made efforts to extend membership down to  $0.1M_\odot$ . In both instances, membership was determined by the convergent point method. Furthermore, field star contamination has been estimated for these data sets; Goldman et al. (2013) found that contamination is likely, although decreasing to negligible levels (less than 10%) inwards of 18 pc within the catalogue. Binaries are present as well, and here we assume a binary fraction of 25%, as suggested by Gunn et al. (1988) (this value was also adopted by Röser et al. 2011).

### 2.2. The Praesepe

The Praesepe is the furthest of our target clusters at roughly four times the distance to the Hyades, but also appears similar to the Hyades in both its age and chemical composition. We adopt  $\mu = 6.26$  mag ( $\approx 179$  pc) (Gáspár et al. 2009) and  $A_V = 0.0837$  (Taylor 2006) for modeling Praesepe. The metallicity of Praesepe has been estimated e.g. by Boesgaard et al. (2013) to be  $[\text{Fe}/\text{H}] = 0.12 \pm 0.04$  based on measurements of 11 Praesepe dwarfs; Cummings et al. (2017) found  $0.156 \pm 0.004$  from spectra of 39 Praesepe members.

Our optical data derives from the 24 members tabulated by Madsen et al. (2002). We have cross matched these stars to obtain updated Tycho  $B_T, V_T$  magnitudes via their Hipparcos ID numbers. This has been checked and cleaned of binary and field stars by the catalog’s authors. Here we also impose a  $V_T < 9$  magnitude cut, for the same reasons that we made this cut in our data of

the Hyades (see 2.1).

Additionally, we use the near infrared (NIR) 2MASS  $J, K_s$  magnitudes catalogued by Wang et al. (2014). This data set includes 1040 stellar members in total, ranging from  $M \approx 0.11 - 2.4M_\odot$  acquired via proper motion analysis. A binary fraction of 20-40% is suggested for these members; correspondingly, we adopt a binary fraction of 30%. Furthermore, as noted by Wang et al. (2014), Praesepe members exhibit distinct proper motions from potentially interfering field stars, virtually eliminating confusion between them. The authors estimate that their member list possesses  $\sim 16\%$  non-members (i.e., 862 true members and 168 non-members). Here we also impose a cut to only include stars with  $V_T < 9$ ; focusing on the MSTO, however also lessening the probability of contaminating stars, as contamination is estimated to lessen towards the population’s bright end.

### 2.3. The Pleiades

The Pleiades is closer to us than the Praesepe, at roughly 3 times the distance to the Hyades, possessing an appreciably younger age, as well as a lower metallicity than the previous clusters. Our adopted distance modulus and extinction for this cluster are: 5.64 mag (Gaia Collaboration et al. 2016), or  $\approx 134$  pc, and  $A_V = 0.1054$  (Taylor 2008), respectively. Soderblom et al. (2009) found  $[\text{Fe}/\text{H}] = 0.03 \pm 0.05$  from spectroscopic measurements of 20 Pleiads. The age has been estimated by Barrado y Navascués et al. (2004) to be  $130 \pm 20$  Myr using the LDB. From CMD analysis, Meynet et al. (1993) determined 100 Myr by fitting non-rotating isochrones to its higher mass stars. Recently, Dahm (2015) found an age of  $112 \pm 5$  Myr via the LDB, using the evolutionary models of Baraffe et al. (1998, 2015).

Our optical data is again found using the Hipparcos IDs of cluster members reported in Madsen et al. (2002), subsequently cross matched for  $B_T, V_T$  magnitudes. Binary and field stars have been removed from this sample by Lindegren et al. (2000) with a maximum likelihood estimation to determine likely (single) cluster members.

We also use the 2MASS magnitudes of members reported by Stauffer et al. (2007). In fitting this data, we only include stars with  $K_s < 5.0$  mag, for the same reasons that we made similar cuts in the Praesepe and Hyades (see 2.1). There is no estimate of binary fraction for this data but stars in this magnitude range are well known, higher mass members of the Pleiades. They are: Alcyone, Electra, Atlas, Maia, Merope, Taygeta, Pleione, and Celeno – many of these are Be stars. Of the stars listed, Atlas is a double line spectroscopic binary system

**Table 2**  
Model Mass, [Fe/H], and Rotation Rate Range

Mass Range	[Fe/H] Range	$\frac{\Omega}{\Omega_c}$ Range
0.1 - 8.0 $M_\odot$	-0.75, -0.60, ..., 0.45	0.0, 0.1, ..., 0.6

(Zwahlen et al. 2004); evidence from lunar occultation (Richichi et al. 1994) suggests Taygeta may be a binary system; Pleione may be a single line spectroscopic binary (see e.g. Katahira et al. 1996 and Nemravová et al. 2010); Electra’s multiplicity is inconclusive thus far, with contradicting evidence (e.g. Abt et al. 1965 and Pearce & Hill 1971); meanwhile Alcyone is a multiple star system, although most of its members are further than 77 arcsec (as listed in the Washington Double Star Catalog). In practice, we assume Atlas and Taygeta are systems whose photometry may be significantly affected by their companions and remove them. We make cuts in our optical data similar to the infrared data, only using stars with  $V_T < 5.0$ .

### 3. METHODOLOGY

Here we give an overview of our models and the fitting procedure from which we derive population age and metallicity. In §3.1, a brief overview of the background physics in our stellar models is given and the effects of rotation and gravity darkening are discussed. Following this, §3.2 introduces MATCH (Dolphin 2002), which we used to turn our stellar models into composite stellar populations. Our fitting procedure is also done via MATCH, fitting composite stellar populations to data, with an outline of its fitting procedure given in §3.3, along with mock tests performed to demonstrate its accuracy.

#### 3.1. MESA Stellar Models

Our models are fundamentally based on the MESA stellar evolution code (Paxton et al. 2011, 2013, 2015, 2018). MESA is a 1D, open source, parallelized code, written with a modular design for flexibility in customizing its incorporated physics. The stellar structure and composition equations are simultaneously solved via a Newton-Raphson solver. Boundary conditions are necessary for solving stellar structure equations; MESA provides a number of options for their choice. In these models, the ATLAS12 code (Kurucz 1970, 1993) model atmosphere tables set these boundary conditions; as done in Choi et al. (2016). Furthermore, we use the protosolar abundances of Asplund et al. (2009) where metallicities are scaled to  $Z = Z_{\odot, \text{protosolar}} = 0.0142$ . In §3.1.1, we give an overview of how rotation manipulates a star and §3.1.2 is dedicated to a description of gravity darkening and how it is implemented in our stellar models.

In this work, we have expanded upon the grids presented in Choi et al. (2016) by computing a set of models with fine variation in initial rotation rates and a denser grid in metallicity. These are not fully evolved, but truncated to the end of core helium burning (CHeB), with a metallicity range more focused on the solar neighborhood and LMC. Our metallicity range has a higher resolution around values appropriate for our clusters of interest (near solar [Fe/H] = 0.0). These choices were made to

introduce greater variability in rotation rate as a model parameter while maintaining a reasonable model creation timescale. The mass, [Fe/H], and rotation ranges covered by our models are listed in Table 2.

#### 3.1.1. Stellar Rotation

In this section we provide a brief overview of the key physical processes related to modeling stellar rotation. See Choi et al. (2016) and the MESA papers (Paxton et al. 2011, 2013, 2015, 2018) for details. In MESA, surface magnetic effects are not modeled, thus magnetic braking is neglected presently. To compensate and reproduce the observed slow rotation of solar-like stars, models below  $1.2M_\odot$  do not rotate. Between  $1.2$  and  $1.8M_\odot$ , rotation is scaled by a factor ranging from 0 to 1 as mass increases, such that models above  $1.8M_\odot$  rotate at their full velocity. For reference: MSTO masses range from  $\sim 1.4 - 2.5M_\odot$  at isochrone ages of 650 – 750 Myr (e.g. the Praesepe and Hyades), and from  $\sim 2.4 - 4.5M_\odot$  at ages of 100 – 150 Myr (e.g. the Pleiades), in our modeling.

Rotational velocity is commonly characterized by the ratio  $v_{\text{ZAMS}}/v_c = \Omega/\Omega_c$ . This is the zero age main sequence (ZAMS) surface equatorial rotation rate,  $v_{\text{ZAMS}}$ , compared with the critical rotation velocity,  $v_c$ , the velocity that would disrupt the star through centrifugal force. The quantities  $\Omega$  and  $\Omega_c$  are the angular counterparts.

The 1D code, MESA, implements rotation through the shellular approximation described by Kippenhahn & Thomas (1970), and employs the diffusive approximation introduced by Endal & Sofia (1978) to model rotationally enhanced chemical mixing. The latter scheme requires that a choice be made for two parameters:  $f_c$ , which dictates how closely compositional mixing follows the flow of angular momentum transport, and  $f_\mu$  which encodes the efficiency of rotational mixing in the presence of stabilizing molecular weight gradients. Values of  $f_c = 1/30$  (calibrated to reproduce the surface  $^7\text{Li}$  abundance of the Sun by Pinsonneault et al. 1989; Chaboyer & Zahn 1992) and  $f_\mu = 0.05$  (found by Heger et al. 2000 to reproduce nitrogen surface enhancement in evolved 10-20  $M_\odot$  stars from Gies & Lambert 1992; Herrero 1993; Vrancken et al. 2000) are adopted in our models.

Although the shellular approximation is virtually ubiquitous in 1D stellar evolution codes, the diffusive approximation is not. Other codes, such as Geneva (Ekström et al. 2012) take a diffusive-advective approach (as described in Maeder & Meynet 2000a) instead. Consequently, MESA models can exhibit noticeable distinctions from models developed via alternative codes, in some respects (as pointed out by Choi et al. 2016, primarily showcasing the differences of higher mass models). Rotating MIST models tend to be fainter and cooler at the MSTO compared to those same models computed by Geneva, perhaps due to less efficient chemical mixing from rotation effects.

In Figure 1 we reiterate these points, focusing on lower and intermediate masses, as would likely be found in our relatively young target clusters. In these plots we show evolutionary tracks for stellar models of 2, 3, 4 and  $7M_\odot$ . Our models are displayed as solid lines, while dashed lines correspond to Geneva models. Rotation rate is encoded by color, wherein red represents  $\Omega/\Omega_c = 0.0$  (non-

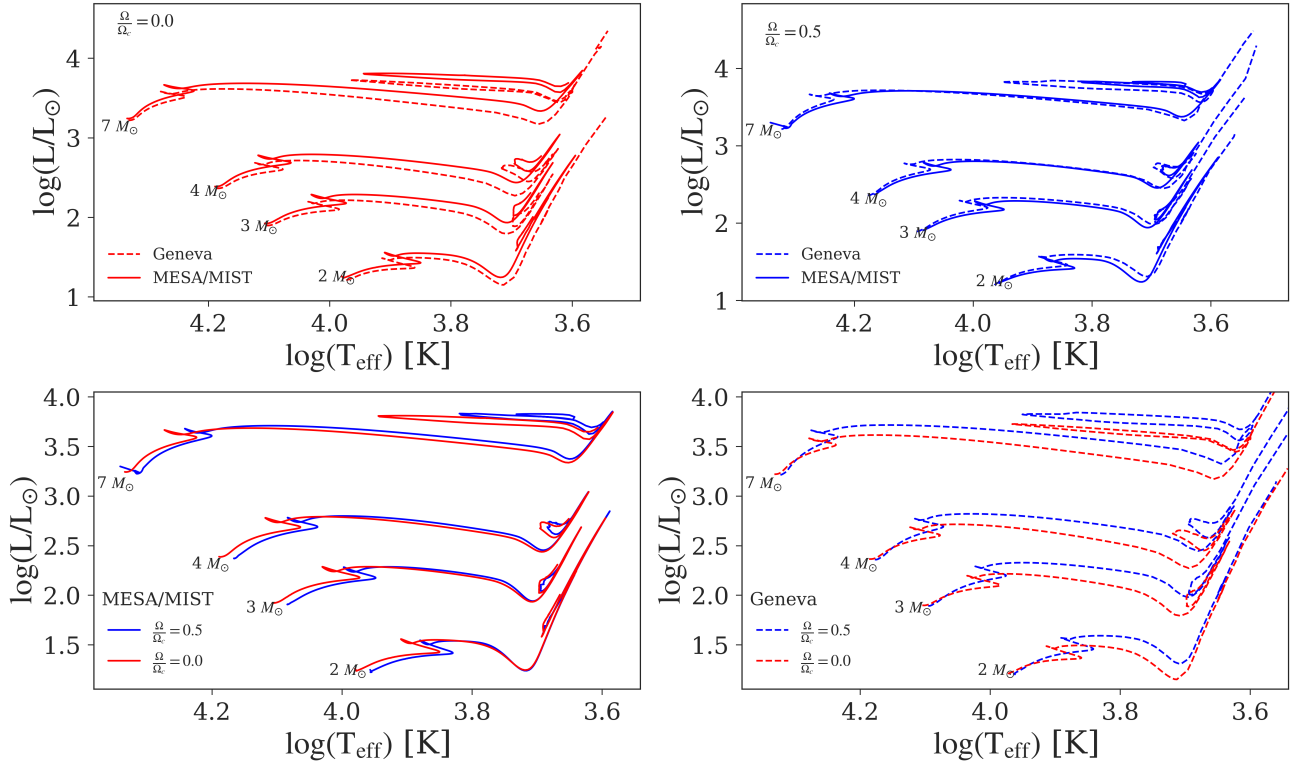


**Figure 1.** Evolutionary tracks of our stellar models in comparison to corresponding Geneva models, displaying model differences between the two codes. The solid red (blue) lines are MIST non-rotating (rotating) models, while dashed blue (orange) lines are Geneva models. Rotating MIST models tend to be fainter and cooler than their Geneva counterparts. (All tracks have  $i = 0^\circ$ , i.e., viewing at the equator.)

rotating) and blue is  $\Omega/\Omega_c = 0.5$ . The two top panels overlay our models and Geneva models with no rotation (top left) and with rotation (top right); these top panels are comparisons across model sets. Our non-rotating models are brighter and hotter than non-rotating Geneva models, however the roles are reversed in comparing rotating models. The two bottom panels compare non-rotating to rotating models within each model set to see how rotation affects the models differently according to each respective code. Our models become cooler as the rotation rate increases (due to gravity darkening; §3.1.2), whereas Geneva models become hotter and brighter as their rotation rate is increased.

Figure 2 shows these effects on a CMD, as they manifest in the MSTO of an isochrone constructed from our models. Figure 2 shows a  $\Omega/\Omega_c = 0.0$  isochrone (black) compared to a  $\Omega/\Omega_c = 0.6$  isochrone (red, dashed) at an age near what has been classically reported for the Pleiades,  $\sim 100$  Myr, (left panel) and an age near classical reports for the Hyades/Praesepe,  $\sim 600$  Myr (right panel). The effects are visually quite different between these ages. On the left, a slightly younger isochrone is shown in solid blue to point out how rotation can enhance the MSTO brightness, causing an older rotating population to mimic the morphology of a younger non-rotating one; here our rotating models might predict older ages compared to non-rotating models (albeit, the effect is very slight in our modeling). Whereas on the right, less massive and more slowly rotating stars exist on the MSTO at 600 Myr and the effects of rotation are modest. Thus, the MSTO barely becomes brighter at these older ages, and primarily appears cooler, mimicking the color-

position of an older population (shown as blue in the righthand panel); here our models might find a younger age (decreasing age will make the MSTO hotter again) than predicted by non-rotating models, or could cause shifts in derived metallicity. Hence, our models do not behave as straightforwardly as Geneva models, where rotation primarily makes the MSTO brighter and hotter. The behavior exhibited by Geneva models leads to rotating models predicting younger ages than non-rotating models.

At 100 Myr, MSTO stellar masses are  $\sim 2.4 - 4.5M_\odot$ , which rotate fully. Meanwhile at 600 Myr, the extant MSTO mass range is roughly  $\sim 1.4 - 2.5M_\odot$ . As discussed at the start of this section, stars below  $1.8M_\odot$  do not rotate at full capacity in order to replicate the effects of magnetic braking relevant to lower mass stars with convective envelopes. Thus, the effects of rotation on MSTO morphology do change with age for our models.

That rotating MIST models are cooler and less luminous than their Geneva counterparts (top right panel, Figure 1) may stem from divergent approaches to rotationally induced angular momentum transport (such differences were also pointed out by Choi et al. 2016). Meanwhile, non-rotating MIST models appear more luminous than those of Geneva (top left panel, Figure 1), perhaps due to differing assumptions made for the treatment of convection.

Convective core overshoot (CCO) mixing is a chief aspect of convection that can influence the MSTO’s CMD morphology and position. CCO is the idea that convectively driven material should not suddenly stop at the

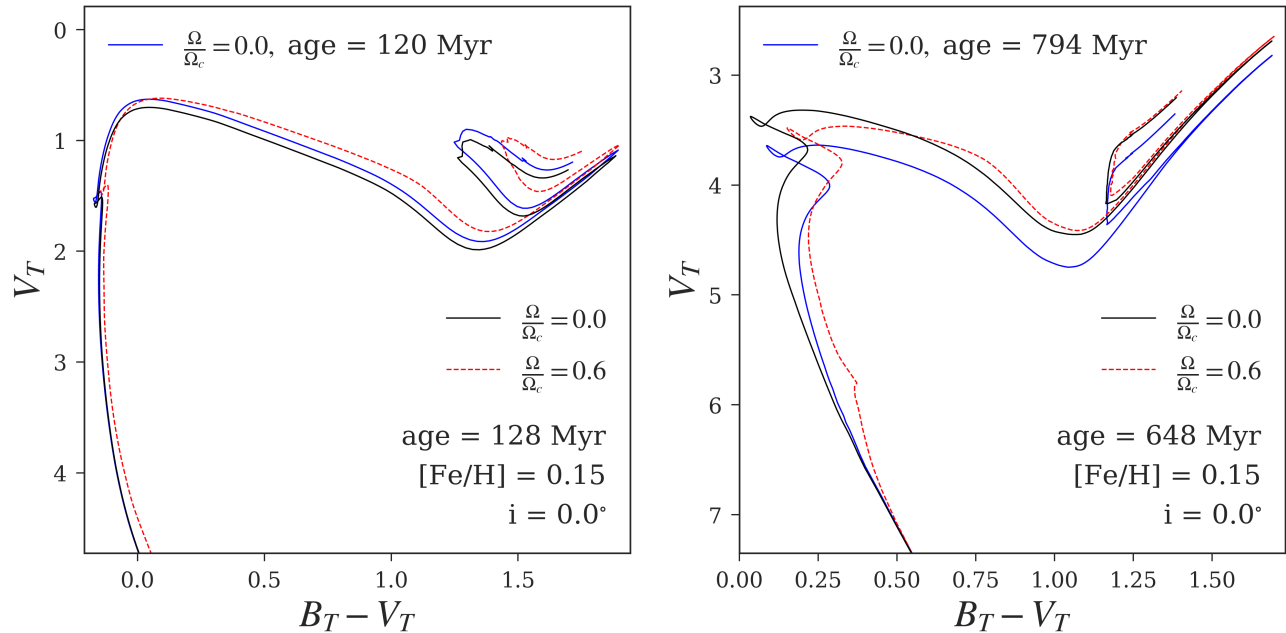


**Figure 2.** Displaying the effects of increasing  $\Omega/\Omega_c$  from 0.0 to 0.6 on a  $[\text{Fe}/\text{H}] = 0.15$  isochrone. The case of a younger age near what is suggested for the Pleiades is shown at left, the case of an older age near classical suggestions for the Hyades and Praesepe at right. In each panel, a non-rotating isochrone is displayed in solid black to compare with a rotating model at  $\Omega/\Omega_c = 0.6$  (red, dashed). In the left panel, increasing  $\Omega/\Omega_c$  from 0.0 to 0.6 causes the non-rotating population to move towards resembling a younger population (blue, solid). In the right panel, increasing  $\Omega/\Omega_c$  creates a cooler MSTO, similar in color to an older, non-rotating population (blue, solid); although the rotating population remains brighter than this older, non-rotating population. (All models have  $i = 0^\circ$  here, i.e., viewing at the equator.)

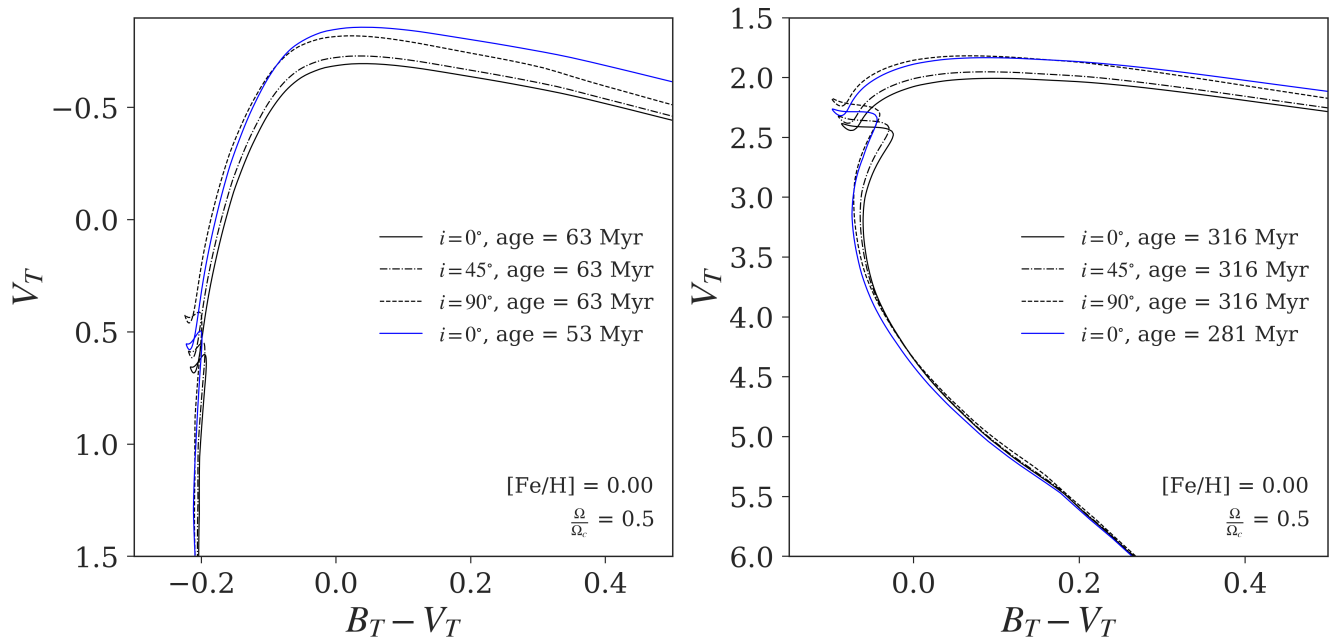


**Figure 3.** Demonstration of the effects of gravity darkening on a CMD, meant to demonstrate general trends of the effects. Gravity darkening is viewing angle dependent and can issue an alteration of several mmag in color and 0.2 mag in brightness. The cases for viewing angle  $i = 0^\circ$  (equator, solid),  $i = 45^\circ$  (dash-dot), and  $i = 90^\circ$  (pole, dashed) are shown. In affecting both the luminosity and temperature of stars, these effects can make MSTO stars appear younger than they intrinsically are. A slightly younger isochrone at  $i = 0^\circ$  is shown (blue, solid) for comparison.

theoretical boundaries (e.g., Schwarzschild or Ledoux) of a convective zone. Rather, it seems feasible that momentum should carry material past these boundaries, allowing it to penetrate into non-convective zones, see e.g., Böhm (1963). The penetration distance, often considered as an extension of the convective zone, is often either

a fraction of the pressure scale height (denoted  $H_P$ ), or is modeled as a diffusive process with an exponentially decaying diffusion coefficient. We adopt the latter formalism, while Geneva adopts the former. Our adoptions (see §3.6.1 of Choi et al. 2016) are roughly equivalent to an extended convective core boundary of  $0.2H_P$  (§2.1 of

Magic et al. 2010), effectively twice the value adopted in Geneva.

Similar to rotationally enhanced mixing, CCO mixing can supply the stellar core with more fuel, enhancing energy production and the MS lifetimes of stars (e.g., Maeder 1975), thereby affecting a population’s MSTO on a CMD. A studies presented by Gallart et al. (2003); Woo et al. (2003) and Bertelli et al. (2003) looked at the intermediate age clusters NGC 2173, SL 556, and NGC 2155, with non-rotating Padova (Girardi et al. 2000) and Yonsei-Yale (based on tracks from YREC, Guenther et al. 1992) stellar models. Modifying the efficiency of CCO appeared to provide one avenue for the models to explain the observed CMD features. Although, an alternative perspective on CCO is that material outside the convective core (CC) boundary, once mixed via overshoot or some other process, may drive an increase in opacity or erasure of composition gradients, subsequently turning sub-adiabatic material super-adiabatic, and expanding the CC (discussed further in §2 of Paxton et al. 2018). CCO may partly be the result of a poorly defined CC boundary in our models. The proper treatment of CCO (and convection in general) is another active branch of development in stellar modeling.

Of course, CCO is not a rotational effect, but is discussed here to expound on the behavior shown in Figure 1 and to highlight its important (albeit uncertain) role in stellar evolution. Our models possess a stronger mixing due to CCO (see Choi et al. 2016, §3.6.2, and Ekström et al. 2012, §2.3). As CCO mixing occurs regardless of rotation, this is a possible cause for our non-rotating models maintaining a higher luminosity than their non-rotating Geneva counterparts.

In addition to the differences shown here on a Hertzsprung-Russell diagram (HRD) and CMD, there are also differences in the MS lifetime extension afforded by enhanced rotational mixing. These differences were shown in Figure 20 of Choi et al. (2016) where the ratio  $\tau_{\text{MS,R}}/\tau_{\text{MS,NR}}$  (MS lifetime with rotation over the same without rotation) is plotted against the initial stellar mass  $M_i$  (in units of  $M_\odot$ ). Rotating Geneva models with  $M_i > 2M_\odot$  show a lifetime extension of roughly  $\sim 25\%$ , while corresponding MIST models only garner an increase of  $\lesssim 10\%$ .

The physical adoptions made in Geneva do not equate to those made in MIST. The uncertainties present in stellar modeling (convection and rotationally enhanced mixing here; see, e.g., Salaris & Cassisi 2017 for a review) provide enough leeway for inconsistent model behavior. As will be seen, our findings are different from what was found in Brandt & Huang (2015a,b), likely due to model differences.

### 3.1.2. Gravity Darkening

In addition to enhanced chemical mixing, rotation also introduces oblateness to stellar structure. Latitudinally dependent centrifugal forces result in an oblate deformation of the star. The surface gravity,  $g$ , of a star is lessened by these forces leading to an effective, latitudinally dependent value,  $g_{\text{eff}}(\theta)$ . Here,  $\theta$  refers to the polar angle in a spherical coordinate system. The effective gravity of a rotating star is related to its radiative luminosity (e.g., as encapsulated by the von Zeipel theorem; von Zeipel 1924), leading to a relation  $g_{\text{eff}} \propto T_{\text{eff}}^4(\theta)$

between the effective gravity and temperature of a star. Hence, the observed colors (temperatures) and magnitudes (luminosities) become dependent on the viewing angle of observation. This effect is commonly termed gravity darkening.

The essential physical arguments of von Zeipel (1924) qualitatively adhere well to observations, but the power law relation presented in the von Zeipel theorem may be too simplistic. As it was derived based on radiative flux relations, the von Zeipel theorem does not directly apply to stars with convective envelopes; Lucy (1967) derived a more general  $g_{\text{eff}} \propto T_{\text{eff}}^\beta$ , with  $\beta = 0.08$  for convective stars. More recently, in comparison to interferometric observations of rapidly rotating stars (McAlister et al. 2005; Aufdenberg et al. 2006; van Belle et al. 2006; Zhao et al. 2009) it has been found that  $g_{\text{eff}} \propto T_{\text{eff}}^4$  over estimates temperature variation going between pole and equator. In light of this, Espinosa Lara & Rieutord (2011) were motivated to derive a new formulation that can describe gravity darkening; they do so, deriving a relation that depends only the rotation rate of the star, at a given viewing angle, luminosity, and  $T_{\text{eff}}$ .

We use the equations of Espinosa Lara & Rieutord (2011) to translate the model stellar luminosity  $L$  and effective temperature  $T_{\text{eff}}$  across desired viewing angles. The symbol  $i$  denotes the inclination (or viewing) angle in this paper;  $i = 0^\circ$  corresponds to an observation directed at the equator, whereas  $i = 90^\circ$  is directed at the star’s pole.

A demonstration of gravity darkening’s effects is shown in Figure 3 on our MESA models. Several isochrones are displayed for two scenarios:  $\sim 60$  Myr models are shown in the left panel and  $\sim 300$  Myr in the right. In both cases, black shows an older isochrone while blue marks a slightly younger isochrone. The solid black line shows  $i = 0^\circ$ , dashed is  $i = 45^\circ$ , and dot-dashed is  $i = 90^\circ$ . In each case, the MSTO of an older isochrone moves towards mimicking that of a younger isochrone as the inclination angle varies from  $0^\circ$  to  $90^\circ$ , due to the increased luminosity and temperature of the stellar pole. Conceivably, if stars were to host a distribution of various inclination angles, there is the possibility that these effects would create a broadened MSTO.

### 3.2. MATCH Composite Populations

The final models that we fit to data are constructed in MATCH (Dolphin 1997, 2002), a tool used to study resolved stellar populations (e.g. see de Jong et al. 2008; Weisz et al. 2011; Gouliermis et al. 2011). MATCH uses a given set of stellar models (our MESA models in this case) to create its own library of isochrones. These models have a finite resolution in age and metallicity; we have chosen 0.02 dex for both. Thus, it should be noted that there is an inherent spread to the models, as the isochrone parameters do not pertain to delta functions in MATCH. Our composite stellar populations are constructed with the effects of gravity darkening via random viewing angles and we have also developed the ability for our synthetic populations to possess a distribution of rotation rates.

CMDs are populated according to an initial mass function (IMF), describing the occurrence of stellar masses, which are subsequently combined into a composite model

population. For this purpose we specify a Kroupa IMF (Kroupa 2001). Additionally, MATCH is able to consider binary systems when drawing its models, given a binary fraction. Binaries are added according to a flat distribution in mass fraction (i.e., from 0 to 1). So long as both stars are alive in the binary, magnitudes are the sum of fluxes from each star; if the primary has died, the magnitude is of the secondary survivor only. Colors are computed by constructing the magnitude in each filter in this way, and then taking the difference of the magnitudes. MATCH does not model interactions between binary companions. In the following discussion, we will list our adopted values of binary fraction where appropriate (adopted binary fractions are also listed in Table 1).

The ability to model gravity darkening was developed and added to MATCH for this project, where the brightness and temperature of our models are altered according to the equations of Espinosa Lara & Rieutord (2011). These alterations are a function of the model’s viewing angle (which is drawn randomly as it is added to the composite stellar population under construction) and their rotation rate. In order to demonstrate these effects, we have created artificial data sets using the MATCH program “fake”, which generates a set of photometric data for use on a CMD, given some finite period of star formation and metallicity variation. This program is also able to simulate photometric errors, but we take the errors to be zero in all cases, in order to highlight rotation related effects. For this reason, we have also increased model resolution to 0.01 dex in Figures 4 and 5, to lessen the spread due to finite composite population model age and metallicity resolution and create an appearance closer to an SSP.

Effects from gravity darkening are shown in Figure 4, as incorporated in MATCH. In Figure 4, an artificial data set that neglects gravity darkening is shown in black, in comparison to an artificial data set that does model gravity darkening which is shown in red. Several scenarios are demonstrated: the left column shows isochrones with  $\Omega/\Omega_c = 0.3$ , while the right shows  $\Omega/\Omega_c = 0.6$ . Meanwhile, the top row compares the effects of gravity darkening at 794 Myr (nearer to the ages of the Hyades and Praesepe), and the bottom row shows 100 Myr (near the age of the Pleiades). The inclusion of gravity darkening has a much stronger effect at higher rotation rates, issuing a greater spread to the MSTO.

Furthermore, stellar populations likely do not have stars rotating at a fixed value, rather they appear to possess a distribution of rates. Studies such as Zorec & Royer (2012) and Royer et al. (2007) have found evidence for a bimodal distribution of rotation rates for A and low mass B-type stars, with masses estimated around  $1.5 - 3M_\odot$ . This mass range is roughly appropriate for the MSTO stars in our target clusters (mentioned at the beginning of §3.1.1). However, there is evidence that this distribution may change with stellar type, where e.g. B and O-type stars appear to exhibit a singly peaked asymmetric distribution (e.g. Penny 1996; Huang et al. 2010; Ramírez-Agudelo et al. 2013).

For this work, the ability to model a distribution of rotation rates has been incorporated as a new feature in MATCH. We use a Gaussian distribution as a preliminary choice to model these effects. As the rotation rates

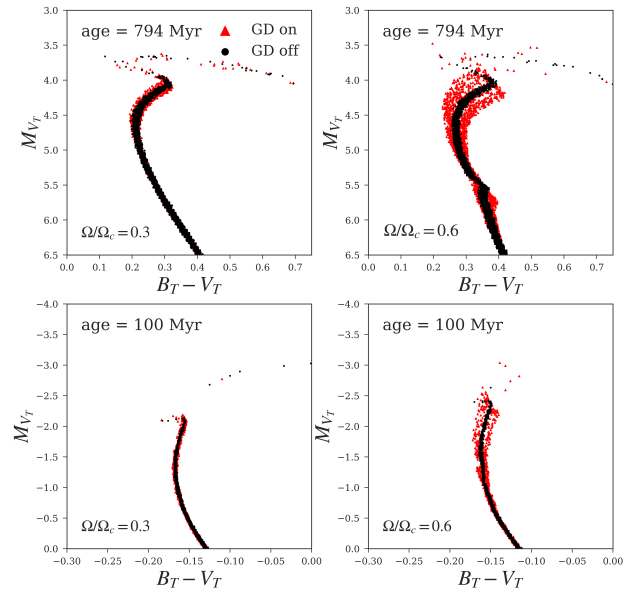


**Figure 4.** Differences between the effects of gravity darkening (GD) at  $\Omega/\Omega_c = 0.3$  (left column) and  $\Omega/\Omega_c = 0.6$  (right column). The effect is stronger for stars that rotate faster, leading to a greater broadening of the MSTO as rotation rate increases. Age is 794 Myr in the top row, 100 Myr in the bottom row, and  $[\text{Fe}/\text{H}] = 0.15$ . These simulated clusters have masses of roughly  $1 \times 10^5 M_\odot$ .

of our models range from  $\Omega/\Omega_c \in [0.0, 0.6]$ , we choose a distribution with mean 0.3 and standard deviation 0.2. This distribution is truncated at the  $\Omega/\Omega_c$  parameter bounds of our model grid; hereafter this distribution is referenced as  $P(\Omega/\Omega_c = 0.3)$ . The rotation rate of a proposed model is drawn from this Gaussian distribution as it is added to the composite population.

Although, as may be seen in Fig. 8 of Huang et al. (2010), for the mass range  $2.2 \leq M/M_\odot \leq 4.0$ , stars may possess a distribution of  $v/v_c$  that is peaked nearer to 0.6 (derived from  $v_{\text{ini}}$  measurements acquired from spectra). This mass range roughly corresponds to the MSTO of the Pleiades, for instance, and so our chosen distribution may not fully represent the distribution of rotation rates in this cluster. In order to test the effects of a distribution that includes higher rotation rates, we have also tested a flat distribution of  $\Omega/\Omega_c$  between 0.0 and 0.6. Given that our models are currently limited to  $\Omega/\Omega_c = 0.6$ , we opt for this rather than creating a new distribution centered on  $\Omega/\Omega_c = 0.6$ . Generally, this flat distribution finds ages within 10 Myr and metallicities very similar to those found with our Gaussian distribution. Our usage of a flat distribution is not an extensive test of a distribution including higher rotation rates, for instance, as may be seen in Fig. 4 the effects of rotation can vary dramatically towards higher rotation rates, so lack of very fast rotators may neglect a wide range of model behavior. However, usage of a flat distribution is intended to give some preliminary sense of whether results would change significantly in the presence of a greater number of fast rotators or not. In future work, we plan to include models from  $\Omega/\Omega_c = 0.0$  to 0.9, allowing us to test a wider range of possible rotation distributions.

In Figure 5, four panels display a progression of the consequences from including gravity darkening (top right), a distribution of rotation rates (bottom left),

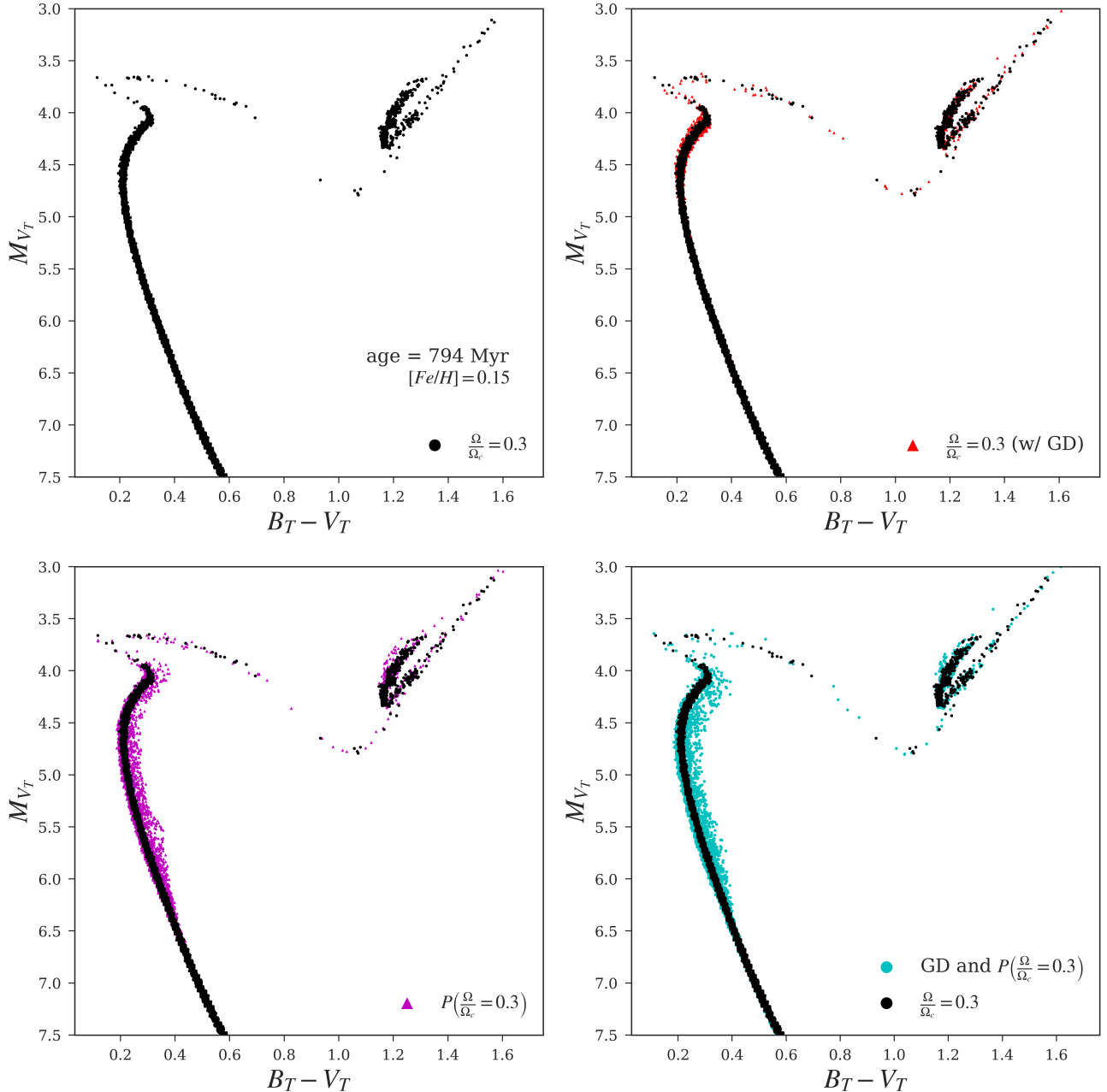


**Figure 5.** Effect of rotation on simulated color-magnitude diagrams. The effects due to including gravity darkening only (top right; GD), a Gaussian distribution of rotation rates (bottom left), and finally the inclusion of both phenomena (bottom right). This is all in comparison to what a model population created through MATCH where none of these effects are modeled looks like (top left), shown in black. All synthetic populations shown correspond either to a singular  $\Omega/\Omega_c = 0.3$  for the population, or to a mean  $\Omega/\Omega_c = 0.3$  in the case of the rotation distribution (with standard deviation 0.2 dex). These models possess a finite age and metallicity resolution: 0.02 dex for each, leading to an inherent spread in their morphologies.

and finally both together (bottom right), in comparison to what a synthetic population looks like in absence of these phenomena (black points). Models excluding a distribution of rotation rates are given the fixed value  $\Omega/\Omega_c = 0.3$ . With the relatively modest value of  $\Omega/\Omega_c = 0.3$ , gravity darkening has a weak influence on MSTO morphology, in comparison to that of a distribution of rotation rates (compare the top right and bottom left panels); although bear in mind that the effects of gravity darkening would increase with  $\Omega/\Omega_c$ , as was shown in 4.

### 3.3. CMD Fitting

Here we present our CMD fitting methodology. First, we describe MATCH and give an overview of its operation in fitting stellar models to data (§3.3.1). Next, we discuss mock tests that were performed to demonstrate the accuracy of our results, using simulated observations that have stellar densities similar to our target clusters (§3.3.2).

### 3.3.1. MATCH

CMD fitting is carried out via MATCH (Dolphin 1997, 2002). This package includes the ability to fit for star formation histories and key population parameters (metallicity, distance, extinction). We exploit these capabilities to determine the age and metallicity of our target clusters, fixing distance and extinction to values based on existing literature. We do not solve for star formation history, instead running MATCH in “ssp” mode, solving for simple stellar populations (SSPs; populations assumed to form all stars in one burst of star formation, as is often assumed for open clusters).

With a given photometric data set (color and magnitude), and a collection of stellar models (MESA in our case), MATCH generates and compares Hess diagrams of the models and data. The model (i.e., synthetic stellar population constructed from supplied models) that best reproduces the observed stellar densities in the CMD space of the data is found with a Poisson likelihood statistic. This is calculated binwise in the Hess diagram, and combined to produce an overall likelihood for the model-data comparison.

Hess diagram bin size is specified by the user, and though guidelines exist, this aspect of the fitting process ultimately involves a degree of personal judgment. Generally, one wants to avoid choosing a bin size so large that the Hess diagram smooths out morphology in important features (like the MSTO), and not so small that spurious population features arise due to outliers, for example. We set a bin size of 0.10 in magnitude and 0.05 in color.

We derive two sets of ages and metallicities in this work. When deriving fits, we always include the effects of gravity darkening and rotationally enhanced chemical mixing. One set of results purely examines how the effects of stellar rotation on derived age and metallicity as rotation rate,  $\Omega/\Omega_c$  is varied. This is important since, as shown in Figure 4, if the majority of stars rotate near  $\Omega/\Omega_c = 0.6$ , the effects of gravity darkening can be much greater. Our other set of results examines what happens when assuming a distribution of rotation rates. Our adopted distribution is a Gaussian, described in §3.2.

In fitting populations at a fixed rotation rate, we fit seven populations constructed with a single value from  $\Omega/\Omega_c \in [0.0, 0.6]$  (steps of 0.1 dex) separately. We select the population that produces the highest maximum posterior probability from these seven models as the best-fit. To examine the case where stars possess a Gaussian distribution of rotation rates (described in §3.2), we simply take the set of best-fit age and metallicity that produces the highest posterior probability according to this model, providing a second set of derived age and metallicity.

### 3.3.2. Testing Parameter Recovery with Mock Data

Here we perform a number of mock tests in order to demonstrate the level of accuracy that MATCH may achieve in fitting our models to data. A rotation distribution and the modeling of gravity darkening are new additions to MATCH, and our data is fairly sparse in comparison to what MATCH is typically used for. Thus, we apply our models to an artificial data set (described below) and test for the ability of MATCH to recover the

input age and [Fe/H] values used to construct this artificial data. We vary the number  $N$  of artificial data points (i.e.,  $N$  is the number of stars in our artificial data) to test accuracy as the observations become more sparse.

An artificial data set with parameters similar to the Hyades, namely:  $\log \text{age} = 8.90$ ,  $[\text{Fe}/\text{H}] = 0.15 \pm 0.01$ ,  $\mu = 3.34$ ,  $A_V = 0.0031$ , was fit using our models in conjunction with MATCH. The artificial data is created using the previously mentioned MATCH program “fake”. In these tests, our artificial clusters contain no multiplicity, and so our binary fraction is set to zero. Below are the results of several trial runs, fitting for the artificial cluster age and metallicity.

Figure 6 shows the results of these mock tests. Here we plot the best-fit age (top row) and metallicity (bottom row) vs.  $N$ , where each point represents an average of 10 trial runs (to average over stochastic fluctuations). Red points correspond to models assigned a single rotation rate, fit to artificial data at a single rotation rate. Blue points correspond to models where a Gaussian distribution of rotation rates was used, fit to artificial data created with a Gaussian distribution of rotation rates. Errors shown are the average errors of the 10 trial runs. These errors were calculated via analysis of resultant posterior probability distribution, marginalized for the corresponding parameter; i.e., from the 16% and 84% percentiles of the posterior. The true values are represented by the light blue horizontal band, bounded by dashed black lines. For these tests, we are using the same models that will be used to fit the observations of our target clusters, which have a resolution 0.02 dex in age and metallicity. We create stars in a single formation episode whose duration in time and spread in metallicity is 0.02 dex (matching the resolution of our model composite stellar populations). Hence, the input age and metallicity bins, represented by the blue bands in Figure 6, span from  $\log \text{age} = 8.90$  to 8.92, and  $[\text{Fe}/\text{H}] = 0.14$  to 0.16 dex, respectively.

Ranging from artificial clusters comprised of several hundred to several thousand total stellar members, the input cluster parameters are often found, or are off by at most 0.05 dex or so. This range in stellar numbers is chosen to replicate that of our target clusters. For instance, our sample of the Hyades contains lists of roughly one to several hundred stars in optical and NIR, respectively; the Pleiades lists contain several hundred; our list for the Praesepe consists of only 24 stars at the cluster turn off in the optical (although with  $\sim 1000$  total members in infrared for Praesepe). As seen in Figure 6, log age appears to not be recovered well in 2MASS  $J$ ,  $K_s$  for the case  $N = 100$  or so. However our NIR data lists contain nearer to 1000 total members.

Models become more degenerate in age and metallicity with fewer total stars, as both the MSTO and MS become less populous under IMF sampling. Accordingly, it is expected that the recovered parameter uncertainties should become larger as  $N$  is decreased, as may be seen in Figure 6. Still, the error bars remain relatively small (of order  $\lesssim 0.03$  dex for log age and [Fe/H] for the worst cases) for results derived with the lowest stellar densities tested here.

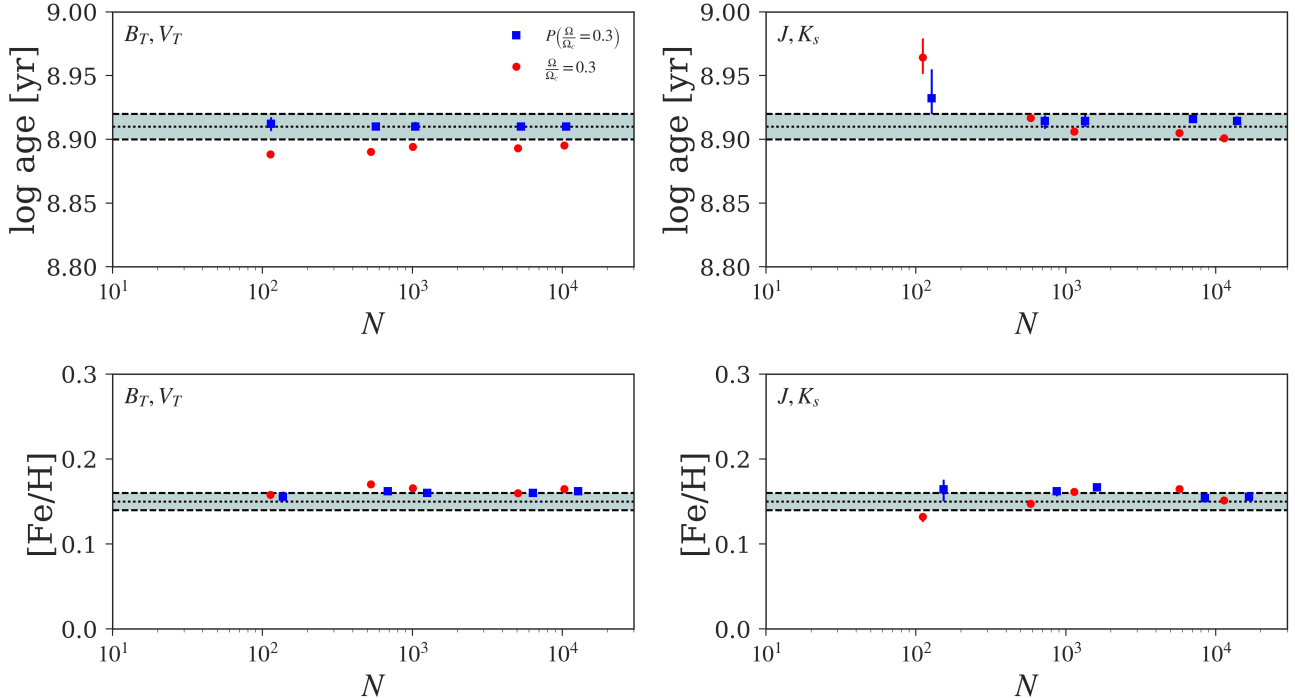


**Figure 6.** Recovery of parameters from simulated CMDs. MATCH best-fit age vs. number of artificial population members,  $N$ , in  $B_T$ ,  $V_T$  (left panels) and  $J$ ,  $K_s$  (right panels). The blue region marks the truth, defined as a burst of star formation taking place between  $\log$  age = 8.90 and 8.92. Likewise, the population metallicity is centered on 0.15 dex, with a 0.02 dex spread in values. Each data point corresponds to an average of 10 trial runs and errors are the average errors of the trial runs. Dotted black lines indicate the middle of an age or metallicity bin.

#### 4. RESULTS

In this section we turn to modeling the benchmark open clusters: the Hyades, Praesepe, and Pleiades, in order to estimate their population ages and metallicities. To this end we utilize a variety of photometric catalogues covering the optical (Tycho  $B_T$ ,  $V_T$ ) and infrared (2MASS  $J$ ,  $K_s$ ), in conjunction with a statistical analysis package, MATCH, which performs the model-data comparison. The adopted distance moduli, extinction  $A_V$ , and binary fractions used to model each cluster are collected in Table 1. We fixed these values and assumed no error in them as they are fairly well determined for these clusters. Errors were calculated via analysis of the marginalized posterior probability distribution (as in §3.3.2) calculated through our fitting procedure (§3.3.1). In several cases, derived metallicities encounter the boundary of our search space ( $[\text{Fe}/\text{H}] = 0.40$ ). Hence, posterior probability distribution is not fully sampled in most cases. For these cases, we report the lower limit in Table 3, defined as the limit containing 68% of the probability in the posterior probability distribution.

##### 4.1. Fitting MESA models to the Hyades, Praesepe, and Pleiades with MATCH

We are exploring the effects that stellar rotation has on derived cluster age and metallicity. With fixed distance and extinction, we fit to the MS and MSTO of the Hyades, Praesepe, and Pleiades. This is performed through Hess diagrams comparing observed to synthetic magnitudes and colors. A pair of results is presented sequentially for each cluster below; derived assuming a single population rotation rate, or assuming a Gaussian distribution of rates (referenced as  $P(\Omega/\Omega_c = 0.3)$ ; §3.3.1).

Figures 7, 8, and 9 show best fitting isochrones overlaid with observed data from the Hyades, Praesepe, and Pleiades. These are representative isochrones from our MESA models; representative in that they exist on model grid points, while the reported best fit values from MATCH belong to a continuum. The displayed isochrone ages are the closest grid point values to the MATCH reports. We have overlaid the Hess diagram of the best-fit  $P(\Omega/\Omega_c = 0.3)$  model in these figures to give a sense of what our models truly look like (shown in gray). For instance, refer back to Figure 5 for the general appearance of our models, with the effects of gravity darkening and a distribution of rotation rates broadening the MSTO.

Best fit isochrones appear to trace the data qualitatively well. Although, in Figures 7 and 8, corresponding to the Hyades and Praesepe, it may be seen that the red clump region in each CMD is not fit very well, perhaps due to complexities in convection (see §5.3). Teal isochrones correspond to fits assuming no distribution of rotation rates. In black, the fit utilizing  $P(\Omega/\Omega_c = 0.3)$  is shown. Solid lines represent isochrones at the best fit values of age and metallicity. Dashed lines are the best fit isochrone at its  $\pm$  uncertainty values in age; these are not displayed with  $P(\Omega/\Omega_c = 0.3)$ , for clarity. Derived errors and best fit values are collected in Table 3.

For the Hyades, we mostly find ages that are consistent with classical non-rotating CMD analyses, and the LDB age determined by Martín et al. (2018), in both filter sets. Metallicities are within  $\sim 0.05$  dex of spectroscopic values. For instance, in  $B_T$ ,  $V_T$ , the age is found to be  $676_{-11}^{+67}$  Myr and  $[\text{Fe}/\text{H}] = 0.23_{-0.02}^{+0.02}$  when modeling a distribution of rotation rates. This age is nearer to results found using non-rotating models, although on the

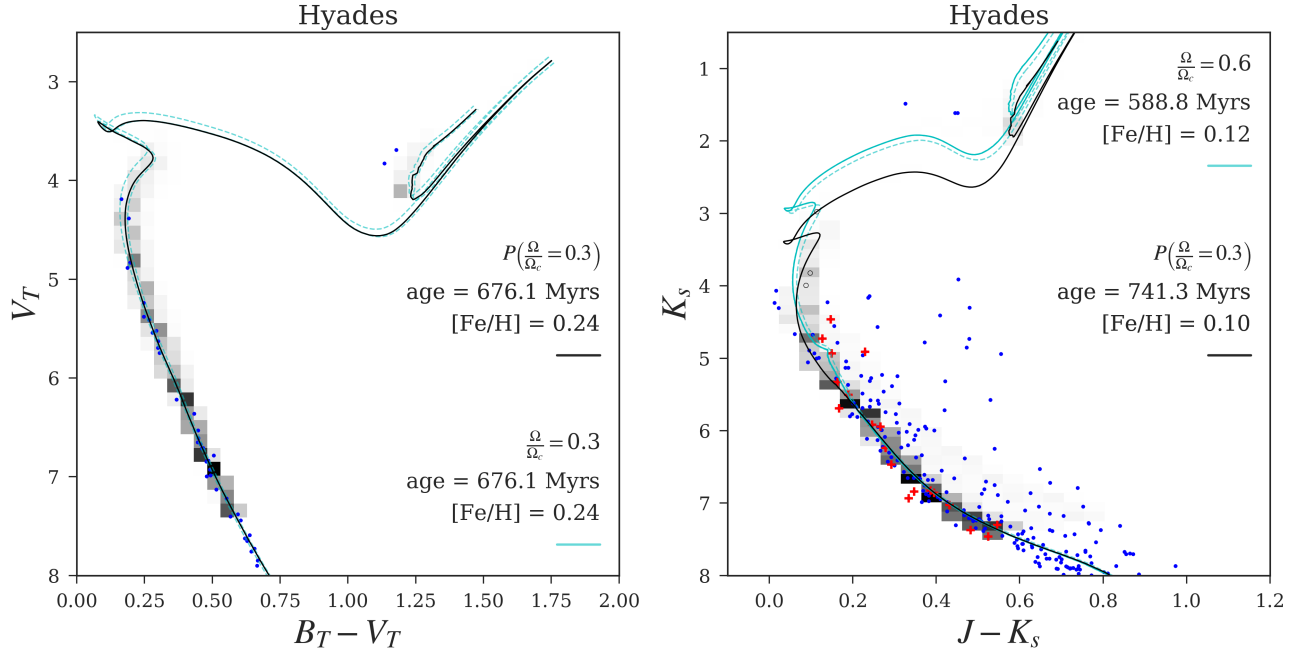


**Figure 7.** Best fit isochrones resulting from our analysis of  $B_T$ ,  $V_T$  (from de Bruijne et al. 2001) is shown at left, and to 2MASS  $J$ ,  $K_s$  data (from Goldman et al. 2013) of the Hyades at right. The best fitting isochrone in absence of a rotation distribution is shown as a solid turquoise line; dashed lines show isochrones at  $\pm$  the uncertainty in best fit age. The black solid line represents the best fit isochrone from parameters derived via the best fit  $P(\Omega/\Omega_c = 0.3)$  model (§3.3.1); the rotation rate of this best fit isochrone is taken to be 0.3, i.e., the  $\Omega/\Omega_c$  value corresponding to the peak of the Gaussian distribution. Red crosses display the right hand side data existent in the left hand side plot, matched on RA and DEC. Open circles (only 3, near the upper MSTO in this figure) represent stars excluded from the fit in MATCH in order to focus on the blueward MSTO stars. The Hess diagram of the best fitting  $P(\Omega/\Omega_c = 0.3)$  model, is overplotted in gray to give a sense of the MSTO spread from rotation effects

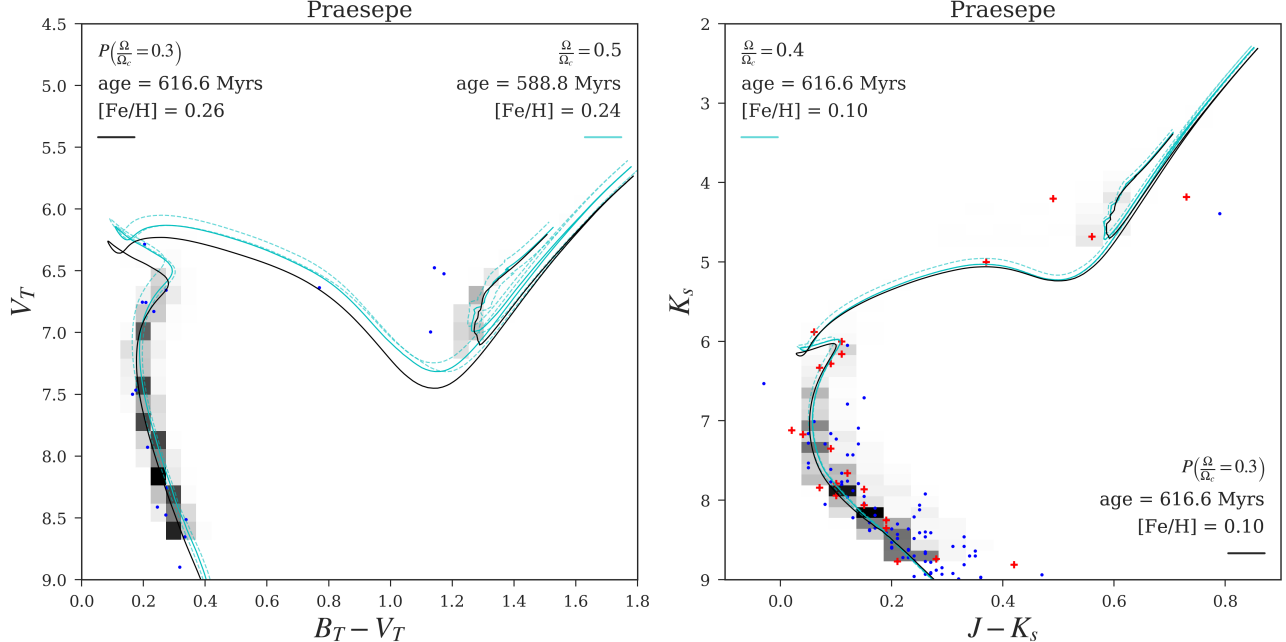


**Figure 8.** Similar to Figure 7, now for the Praesepe. The fit to  $B_T$ ,  $V_T$  (from members listed by Madsen et al. 2002) is shown at left, and to 2MASS  $J$ ,  $K_s$  data (from Wang et al. 2014) at right.

higher end. Ages of  $\sim 680$  Myr are found for the Hyades, whether using a distribution of rotation rates or a fixed value. This is true for the Hyades in all cases, except with our age determined via NIR data when modeling a distribution of rotation rates.

For the Hyades in NIR, when using a Gaussian rotation

distribution, we see an age of  $741^{+55}_{-11}$  Myr. This older age may result from the greater color span of MSTO stars here. In some sense, this resembles a broadened MSTO; using a distribution of rotation rates also makes the MSTO more broad. Thus, the  $P(\Omega/\Omega_c = 0.3)$  model can fit both the redder and bluer MSTO stars by sitting

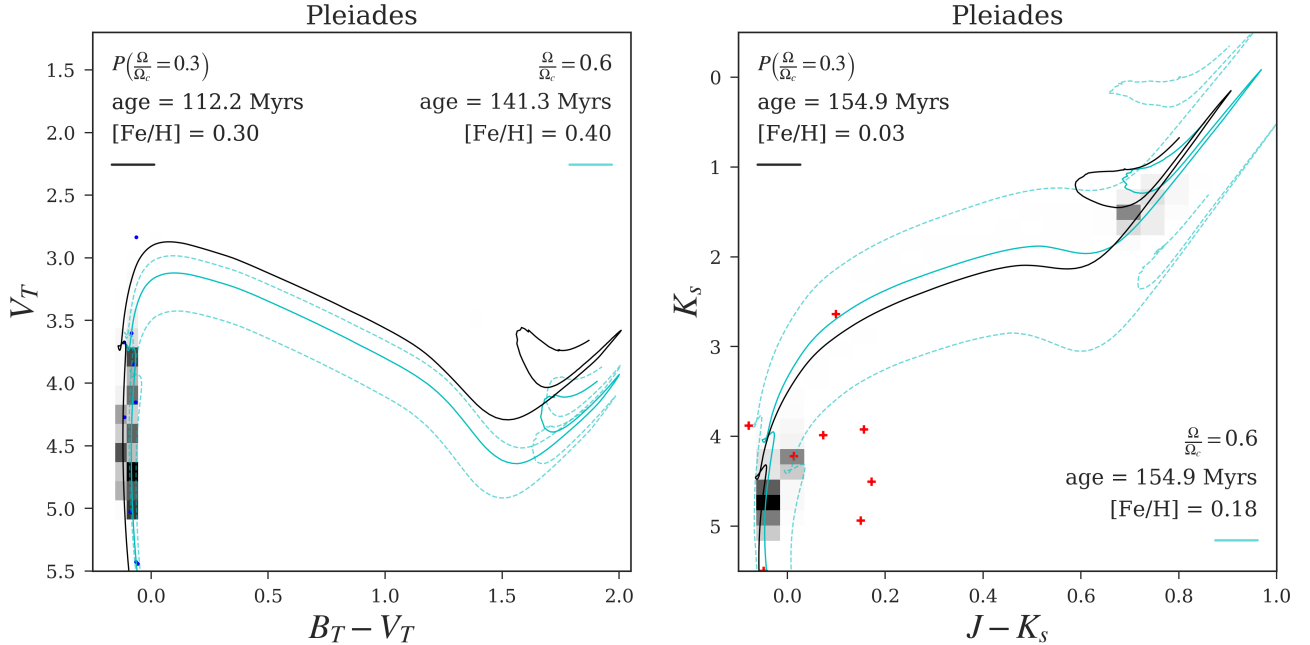


**Figure 9.** Similar to Figure 7, now for the Pleiades. The fit to  $B_T, V_T$  (from members listed by Madsen et al. 2002) is shown at left, and to 2MASS  $J, K_s$  data (from Stauffer et al. 2007) at right.

in the middle, driving an older age than the fixed  $\Omega/\Omega_c$  model, which is forced to fit either the redward or blueward MSTO stars more so. On this point, note that our best fit single  $\Omega/\Omega_c$  model for the Hyades in NIR is high (0.6) compared to the lower value found in optical. This is due to the relatively low color span of MSTO stars in optical compared to NIR for the Hyades; the effects of gravity darkening produce a greater color spread in MSTO stars at higher rotation rates, driving the best fit model its higher  $\Omega/\Omega_c$  value. However, the MSTO spread in this case may be due to complications in the photometry. Membership and binarity uncertainties could be at play here, i.e., this older age could be spurious; (e.g., Kopytova et al. 2016 find a tighter NIR MSTO morphology, identifying single stars in the Hyades). We excluded several of the redder MSTO stars from this fit, indicated in Figure 7 by the open circles (there are 3 on the upper MSTO) in 2MASS  $J, K_s$ . This was done to reduce the influence of redward MSTO stars on derived age here. The Praesepe and Pleiades do not display as large of a color span in their MSTOs with NIR data.

It may also be noted that a much higher value of  $\Omega/\Omega_c$  is preferred in fitting the NIR data of the Hyades (0.6 vs. 0.3 in optical). This is likely due to the MSTO of the Hyades having a greater spread in color and more MSTO stars in the NIR data. Adopting a higher  $\Omega/\Omega_c$  grants models a broadened MSTO, via gravity darkening (e.g., Fig. 4). We speculate that this allows a better fit to the NIR data, but is statistically worse in application to the Hyades optical morphology, which lacks a significant color spread in its MSTO. However, we leave a more thorough explanation of this discrepancy to future work.

Thus, for the Hyades, our ages mostly resemble those of classical non-rotating isochrone determinations, e.g., Perryman et al. (1998). The metallicity results roughly align with the measurement of  $[\text{Fe}/\text{H}] \approx 0.15$  from Cummings et al. (2017), although our results from the optical bands tend to favor values nearer to  $[\text{Fe}/\text{H}] = 0.20$ , while

in NIR we find nearer to  $[\text{Fe}/\text{H}] = 0.10$ .

The situation for the Praesepe is similar to that of the Hyades: we see results nearer to reports from non-rotating models. This is the case across the NIR and optical data sets, whether using fixed  $\Omega/\Omega_c$  or  $P(\Omega/\Omega_c = 0.3)$ . Here, the ages tend towards  $\sim 590$  Myr, while the best fits for  $[\text{Fe}/\text{H}]$  are near  $\sim 0.09$  in the NIR and in  $B_T, V_T$ , we find  $[\text{Fe}/\text{H}] \sim 0.25$ . Here our optical data set contains fewer MS stars than our NIR, making metallicity more difficult to determine, driving higher  $[\text{Fe}/\text{H}]$  values here.

For the Pleiades, we similarly find ages that agree with classical, non-rotating analyses, as well as LDB results. Our ages fall within the range  $\sim 112 - 160$  Myr, in concordance with values derived from the LDB, and non-rotating isochrones. In the NIR, using a distribution of rotation rates, the ages have a large uncertainties. The MSTO of the Pleiades in NIR is relatively more extended, driving this behavior. Values of  $[\text{Fe}/\text{H}]$  range from  $-0.01$  to 0.40 (our  $[\text{Fe}/\text{H}]$  search boundary); these tend to be higher than established values. Similar to the scenario seen with the optical data set for the Praesepe, the number of stars here is very low: only 7. Our magnitude cuts of  $V_T < 5.0$  and  $K_s < 5.0$  were made to focus more on the MSTO, at the expense of constraints from the numerous MS Pleiads.

With the Pleiades, we did attempt fits with less severe magnitude cuts, but this in turn led to an increased age. On a Hess diagram, the low stellar density in the MSTO makes its stars appear as outliers in determining a global fit, despite these few stars being perhaps the most significant to extracting an accurate age. With relatively few stars, our uncertainties on age are larger for this cluster than the others. Moreover, many of the derived metallicities are unbounded and not well determined.

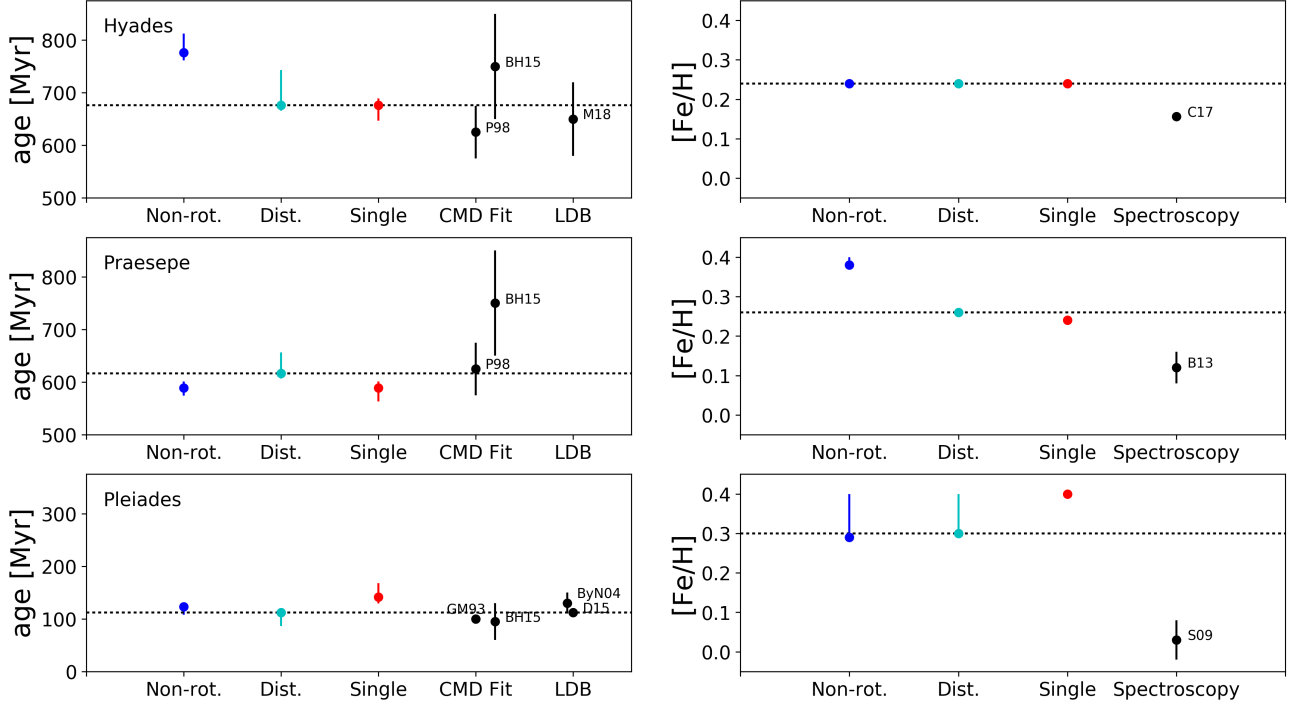


**Figure 10.** Summary of results from Tycho  $B_T$ ,  $V_T$  photometry. Several literature values are displayed in black, alongside our results derived with and without a rotation distribution (turquoise and red, resp. (see §3.1.1 for details on the distribution) for the population; non-rotating results are shown in blue. Literature values above are Perryman et al. (1998) (P98; used non-rotating isochrones), Meynet et al. (1993) (GM93; used non-rotating isochrones), Martín et al. (2018) (M18; used the LDB), Barrado y Navascués et al. (2004) (ByN04; used the LDB), Cummings et al. (2017) (C17; used spectra of 37 Hyads), Boesgaard et al. (2013) (B13; used 11 Praesepe dwarfs), Soderblom et al. (2009) (S09; from spectra of 20 Pleiads), Dahm (2015) (D15; used the LDB). BH15 refers to Brandt & Huang (2015a) and Brandt & Huang (2015c), where rotating Geneva stellar models, interpolated with non-rotating PARSEC models, were fit to MSTO stars of these clusters. The black dotted line is included to aid comparisons of our full model (gravity darkening and rotation distribution) to other results. Unconstrained values in  $[\text{Fe}/\text{H}]$  are lower limits (see text), given an uncertainty reaching to the boundary of  $[\text{Fe}/\text{H}]$  parameter search space: 0.40.

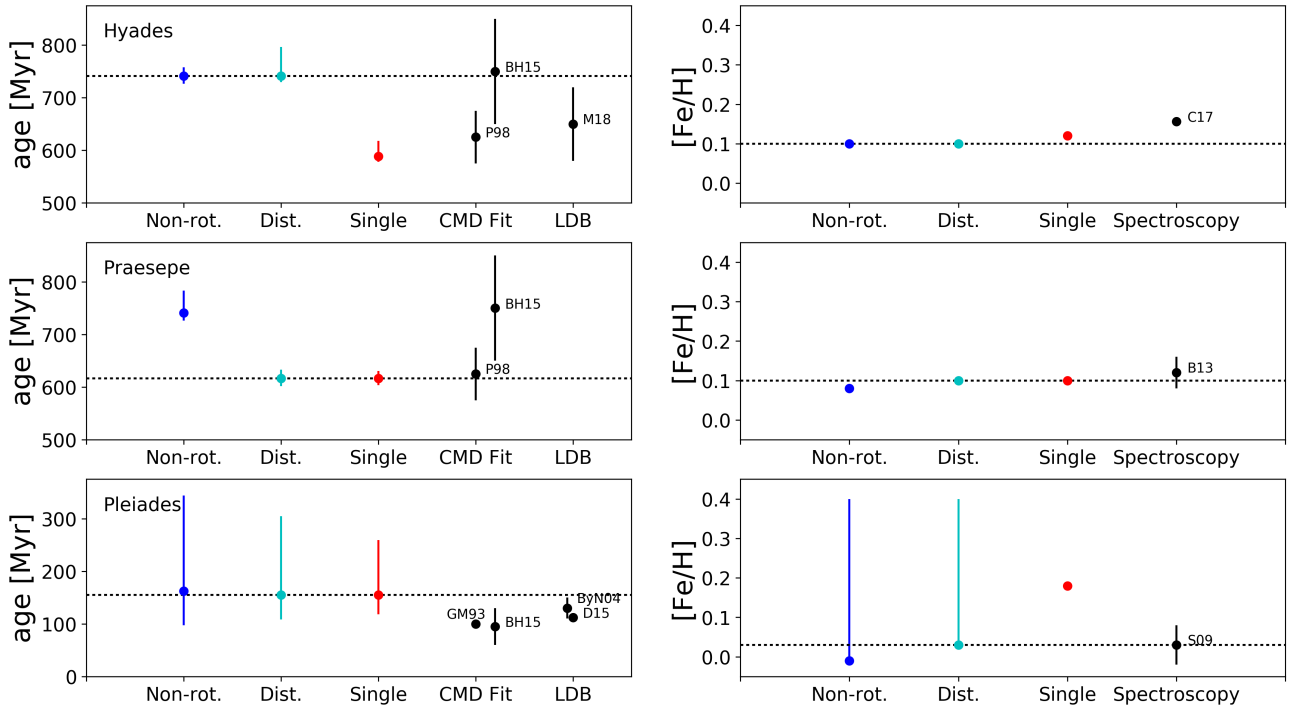


**Figure 11.** Summary of results, but now for 2MASS photometry; see Figure 10 for details. For a discussion on the higher age derived here with the Hyades under a Gaussian distribution of rotation rates, see §4.1.

## 5. DISCUSSION

Here we present a comparison of ages derived in previous literature to our derived ages for the Hyades, Praesepe, and Pleiades in §5.1. Following this is a discussion on our results in comparison to ages derived using rotating models built with the Geneva code, and interpolated with PARSEC stellar models for a greater range in metallicity and finer mass resolution (§5.2). Finally, we discuss the effect of mixing length on the red clump region (§5.3). The red clump’s CMD position is sensitive to the efficiency of convection, and our default models were found to not match this region well; altering the efficiency may be a possible solution, at least in some cases.

### 5.1. Comparison to Literature Ages and Metallicities

Figure 10 shows our best fit age and  $[\text{Fe}/\text{H}]$  from fitting to optical data in comparison to several literature values; Figure 11 shows the same for our infrared data fits. For the Hyades, Praesepe, and Pleiades, we generally find ages that align with classical results (although see §4.1 about the higher age derived for the Hyades in our NIR fit). Our metallicities for the Hyades, Praesepe, in the optical, and the Pleiades in both optical and infrared, appear to be inconsistent with literature values. Metallicity is unconstrained in these cases, leading to a dubious metallicity determination that lies near the end of our search space in metallicity: 0.40 dex. That metallicity appears unconstrained here is probably due to the relatively low stellar number densities present in these data sets, and the issues that this may cause with analysis on a Hess diagram. Additionally, we excluded much of the MS in our fits to the Pleiades, sacrificing its use in constraining metallicity, opting to focus on the sparse, brighter Pleiads for an age determination that is driven more by the MSTO.

The derived ages of the Hyades and Praesepe from CMD analysis using non-rotating isochrones and the LDB congregate near 625 – 650 Myr (see references in §2.1 and §2.2). For the Pleiades, non-rotating isochrone and LDB analysis have derived ages from about 100 – 130 Myr (see references in §2.3). Our ages are consistent with classical non-rotating isochrone CMD fits and LDB results (where available) for the Hyades, Praesepe, and Pleiades.

Our results contrast with the ages derived by Brandt & Huang (2015a) (see e.g., the points labeled BH15 in Figure 10 and 11). Derived ages of the Hyades and Praesepe from CMD analysis using rotating Geneva isochrones, carried out by Brandt & Huang (2015a,c), using a Bayesian approach, are greater than classical reports. An age of  $750 \pm 100$  Myr was derived for Hyades ( $800 \pm 50$  if fixing metallicity to  $[\text{Fe}/\text{H}] = 0.10$ ). The age of the Praesepe was determined to be  $790 \pm 60$  Myr. Lastly, an age of  $\sim 95 \pm 35$  Myr was determined for the Pleiades, consistent with classical non-rotating age determinations and the LDB. Our derived ages agree with these studies for the Pleiades, but we do not find as great of an age increase for the Hyades nor the Praesepe via our models and methods.

The metallicity results for the Hyades and Praesepe are lower by  $\sim 0.05$  dex of literature values in our 2MASS fits; in  $B_T$ ,  $V_T$ , best fit  $[\text{Fe}/\text{H}]$  for the Hyades and Prae-

sepe are higher by  $\sim 0.05$  dex of literature values. Our metallicity results for the Pleiades are generally inconsistent with literature values (those being  $[\text{Fe}/\text{H}] \approx 0.0$ ); this is likely due to our magnitude cuts excluding much of the MS in favor of MSTO stars, and thus  $[\text{Fe}/\text{H}]$  becoming unconstrained in this CMD region. For instance, note the similarity in CMD position of the isochrones in Figure 9 (right panel), although they differ by  $\sim 0.10 - 0.15$  dex in metallicity.

Generally, rotating models are preferred owing to a mildly higher probability over non-rotating models. MATCH uses a Poisson equivalent to  $\chi^2$  as a fit statistic (e.g., see Dolphin 2002, §2.3), designated via  $-2\ln P$  (a lower value corresponds to higher probability), where P is the cumulative Poisson likelihood ratio, incorporating all Hess diagram bins. For the Hyades, we find  $-2\ln P = 104$  in optical photometry for the best fitting model, while the non-rotating model shows  $-2\ln P = 120$ , for instance. The best-fit model with a Gaussian distribution of rotation rates achieved  $-2\ln P = 101$  in this case. Typically, rotating models are preferred according to the fit statistic by roughly 3 – 25% over non-rotating models.

The results derived via models with a Gaussian distribution of  $\Omega/\Omega_c$  or a fixed value are often similar. However, as these clusters contain relatively low stellar densities in their MSTOs, they do not provide a strong distinction between more realistic models that include a distribution of rotation rates, and those that possess a fixed population  $\Omega/\Omega_c$  value. With precise photometry from upcoming data sets like *Gaia* DR2, and in studying more populous clusters such as those in the LMC and SMC, we will have a better opportunity to assess the role of a rotation distribution.

### 5.2. Comparison to Geneva Models

Our models behave differently from Geneva models, as highlighted in §3.1.1, so it may be no surprise that our results differ from work that utilizes the Geneva models. Rotation has more modest consequences for stellar evolution under our physical assumptions, so we do not observe a strong affect on derived ages due to stellar rotation. No major differences in derived age appear to manifest from using a Gaussian distribution of rotation rates as opposed to a single value. Indeed, the MSTOs present in these clusters tend to not be especially well populated, and so any spread that may exist due to a distribution of rotation rates may be difficult to observe.

As rotation tends to make the MSTO primarily cooler in our modeling, at least at ages near 600 Myr (see Figure 2), it makes sense that we do not find a significantly older age for the Hyades or Praesepe. Rather, adopting a younger age would increase the brightness and make the MSTO hotter, helping an isochrone compensate for the effects incurred by an increased rotation rate. Vice versa in the case of the Pleiades at  $\sim 120$  Myr, here increasing rotation primarily makes the models brighter, leading models with higher  $\Omega/\Omega_c$  to mimic younger stars at fixed age<sup>3</sup>.

This is in contrast to results found by Brandt & Huang (2015a), Brandt & Huang (2015c), where the Praesepe

<sup>3</sup> Note the slight increase in luminosity at the MSTO of the  $M > 2M_\odot$  models in Figure 1 and the more apparent enhancement in Figure 2 at  $\sim 120$  Myr.

and Hyades showed an age increase of roughly 200 Myr as a result of stellar rotation in their modeling. In Geneva models, the changes in isochrone morphology due to rotation are almost completely opposite to the effects seen in our models. Geneva models are hotter, brighter, and live longer on the MS (meaning the population evolves more slowly), as discussed in §3.1.1. It seems plausible that this discrepancy may stem from a more modest rotational mixing efficiency in MIST compared to Geneva. Whether this is precisely the case, or perhaps if other model differences come into play more strongly will require further investigation. It is also important to bear in mind that our model set is limited to  $\Omega/\Omega_c = 0.0$  to 0.6 presently, while the Geneva models allow study from  $\Omega/\Omega_c = 0.0$  to 1. Extending our model grid to include  $\Omega/\Omega_c > 0.6$  will be fruitful for comparison, aside from perhaps being necessary to study realistic rotation distributions (e.g., those discussed in Huang et al. 2010); we aim to incorporate models with higher rotation in future work.

Furthermore, our models possess a greater mixing due to CCO. This was shown in Figure 1 to make our non-rotating models hotter and brighter than their Geneva counterparts. The effects of CCO mixing are similar to rotationally enhanced mixing, effectively expanding the stellar core, granting it more fuel to burn longer, brighter, and hotter. Our non-rotating age determinations are near what Brandt & Huang (2015a) found with their rotating models (see Table 3 and Figures 10 and 11). It seems plausible that this is due to the higher level of CCO mixing in our models, as CCO makes the MSTO hotter and brighter. Proper 1D treatment of convection is yet another complication in stellar evolution theory and CMD-based analyses.

The physical assumptions made in our models §3.1 and in Geneva are both able to simulate observational constraints. Much of our adopted physics follow from the assumptions made in MIST (Choi et al. 2016; see §8 and 9 of that paper for comparisons to data), while the physics adopted in Geneva (Ekström et al. 2012; see §5 of that paper for comparisons to data) are similar, although there are differences, for example, in the treatment of rotational mixing and the assumed strength of convective core overshoot mixing. In our adopted formalism, the rotational mixing parameters  $f_c$  and  $f_\mu$  are tuned to match the observed nitrogen enrichment in galactic MS B-type stars (with the observations from e.g., Gies & Lambert 1992; Kilian 1992; Morel et al. 2008; Hunter et al. 2009), following Heger et al. (2000). The Geneva models are capable of reproducing these observed surface abundances without having any parameters calibrated to do so in their formalism, followed from Maeder & Zahn (1998). Thus, although physical assumptions may differ between model sets, neither is ruled out by observational constraints thus far.

### 5.3. Effect of Mixing Length on the Red Clump

Although our fits appear to match the observed MS and MSTO regions relatively well for these clusters, in Figures 7 and 8, it is clear that our best-fit isochrones miss the red clump region. Figure 12 displays the range of convective mixing at various values, to demonstrate how it can affect the red clump region. In particular, we vary the parameter  $\alpha_{MLT}$ , responsible for setting the

enhanced range of convective mixing, according to the Mixing Length Theory (MLT) of Böhm-Vitense (1958). This parameter essentially dictates how far a fluid parcel travels,  $l_{MLT}$ , before mixing thermally with its surroundings; this length scale is characterized as some fraction of the pressure scale height,  $H_P$ , and is related to the constant  $\alpha_{MLT}$  via  $l_{MLT} = \alpha_{MLT} H_P$ .

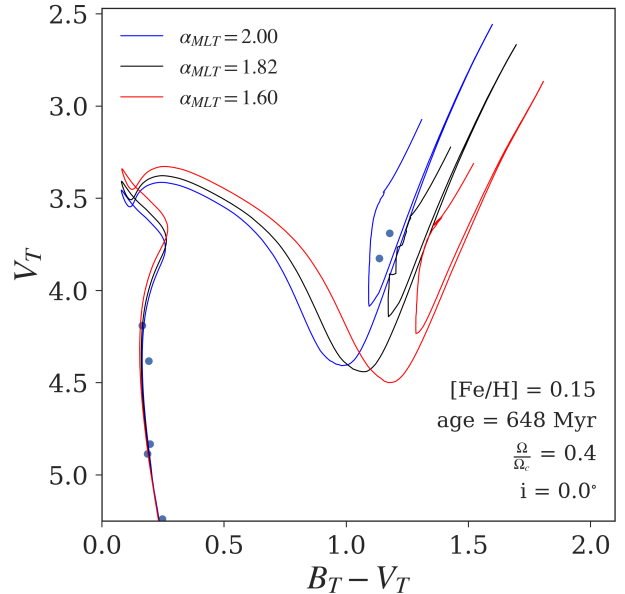


**Figure 12.** Showcasing the effect of altering the convective mixing length parameter  $\alpha_{MLT}$ . The default value of  $\alpha_{MLT}$  is 1.82 in our models (shown as black), calibrated to reproduce solar Li surface abundances. Analogous isochrones are shown at  $\alpha_{MLT} = 1.60$  (red) and  $\alpha_{MLT} = 2.00$  (blue) for comparison. The data featured here is the cross matched data from the member list of de Bruijne et al. 2001 for the Hyades.

By default  $\alpha_{MLT} = 1.82$  in our models, based on solar calibration (discussed further in Choi et al. 2016). Figure 12 shows isochrones, at age 649 Myr (similar to our derived ages for the Hyades and Praesepe),  $[Fe/H] = 0.15$ ,  $\Omega/\Omega_c = 0.4$ , and inclination  $i = 0^\circ$ , at various  $\alpha_{MLT} = 1.60, 1.82$  (default), and 2.00. Altering  $\alpha_{MLT}$  makes the modeled red giant stars hotter or cooler, providing potential for a better fit to a given data set. In Figure 12 it is shown that a greater  $\alpha_{MLT}$  may provide a better fit in the case of the Hyades. However, in the Praesepe this may lead to a worse fit, as it would pull the model away from two of the redder red clump stars.

Some 3D modeling efforts have seen evidence that  $\alpha_{MLT}$  may vary with e.g., stellar  $T_{eff}$ ,  $\log g$ , (Trampedach et al. 2015) and metallicity (Magic et al. 2015). Evidence that  $\alpha_{MLT}$  may vary with stellar parameters has also been seen in comparing models to observations, as in e.g., Bonaca et al. (2012); Tayar et al. (2017); Joyce & Chaboyer (2018); Chun et al. (2018); Li et al. (2018), and Viani et al. (2018). However, Choi et al. 2018 (submitted to ApJ) found that model  $T_{eff}$  can vary by nearly  $\pm 100$  K according to the treatment of surface boundary conditions in 1D codes. Thus, it appears that discrepancies between models and observations may (at least in part) be due to the chosen boundary conditions used in comparing models to data. Determining precisely how  $\alpha_{MLT}$  may vary, and according to which stellar properties, is an

ongoing task. Efforts by e.g., [Arnett & Moravveji \(2017\)](#) and [Mosumgaard et al. \(2017\)](#) will aid in having 3D simulations further inform our 1D models. Convection is another uncertain aspect in stellar modeling, alongside the uncertainties of stellar rotation.

## 6. SUMMARY

In this paper our goal was to explore the effect of stellar rotation on the inferred ages of open clusters, using the well-studied examples of the Hyades, Praesepe, and Pleiades. Our results are summarized here:

- Application of self-consistent rotating isochrones (constructed via MESA) to CMD data of the Hyades, Praesepe, and Pleiades has yielded results that suggest no major influence on derived ages from the inclusion of rotation, even when including the effects of gravity darkening and a distribution of rotation rates (see §3.1).
- Our ages, derived using the statistical analysis package MATCH, are similar to values based on non-rotating models. Our models suggest ages of  $\sim 680$  Myr,  $\sim 590$  Myr, and  $\sim 110 - 160$  Myr for the Hyades, Praesepe, and Pleiades, respectively with our binary cleaned data. Our metallicity determinations roughly agree with literature in cases where the data provides a populous MS (i.e., in NIR for the Hyades and Praesepe, and the optical for the Hyades). These results are collected in Table 3.
- These results are in contrast to the findings of [Brandt & Huang \(2015a\)](#) who used Geneva stellar models, where a marked difference between rotating and non-rotating models was found for the Hyades and Praesepe clusters. In that work, rotation increased population ages by  $\sim 200$  Myr, as derived from the MSTO; our models find a less dramatic increase to derived age.

The physics that we have adopted in our modeling differs from what is adopted in Geneva. Either set of physics is well-founded in that they each are tuned to reproduce certain observations, and can do so successfully. Our models show comparably modest differences as rotation rate is varied; whereas the changes to stellar lifetime, luminosity, and temperature are more dramatic in the Geneva models (see [Choi et al. 2016](#) for additional comparisons). Such model uncertainties complicate the establishment of an age for the Praesepe and Hyades based on CMD analysis. However, it is worth noting that our derived ages agree with what others have found via the LDB method. These results demonstrate a reason for caution in using rotating stellar models. We still contend with significant uncertainty in crucial evolutionary processes (particularly rotation and convection in this context), producing correspondingly uncertain results.

Moving forward, our models are primed to look at how stellar rotation may factor into the eMSTOs observed in LMC and SMC clusters. In future work, we plan to compile and present the predicted star formation histories of several such clusters using the models developed here. Gravity darkening and a distribution of rotation rates

are able to significantly broaden the MSTO (e.g., [Bastian & de Mink 2009](#) and our Figure 5). It may be that rotation is not able to fully explain for the observed eMSTO morphology (e.g., see [Goudfrooij et al. 2017](#)), but our upcoming work aims to assess the extent to which rotation can account for an MSTO spread, according to our models. Given alternate, yet still viable sets of physical assumptions exist in our models, we hope to further elucidate what stellar rotation may be capable of.

## 7. ACKNOWLEDGMENTS

We thank Timothy Brandt for helpful comments and discussion on earlier drafts of this paper. We would also like to thank the anonymous referee for their comments in improving the clarity of the paper. SG acknowledges the National Science Foundation Graduate Research Fellowship under grant No. DGE1745303. CC acknowledges support from NASA grant AST-1313280, and the Packard Foundation. This paper is based upon work supported by the National Aeronautics and Space Administration (NASA) under Contract No. NNG16PJ26C issued through the WFIRST Science Investigation Teams Program. Some of this material is based upon work supported by the National Science Foundation under Award No. 1501205. We would also like to thank Bill Paxton and the MESA community for making this work possible.

## REFERENCES

- Abt, H. A., Barnes, R. C., Biggs, E. S., & Osmer, P. S. 1965, *ApJ*, 142, 1604 [2.3](#)
- Arnett, W. D., & Moravveji, E. 2017, *ApJ*, 836, L19 [5.3](#)
- Asplund, M., Grevesse, N., Sauval, A. J., & Scott, P. 2009, *ARA&A*, 47, 481 [3.1](#)
- Aufdenberg, J. P., Mérand, A., Coudé du Foresto, V., et al. 2006, *ApJ*, 645, 664 [3.1.2](#)
- Baraffe, I., Chabrier, G., Allard, F., & Hauschildt, P. H. 1998, *A&A*, 337, 403 [2.3](#)
- Baraffe, I., Homeier, D., Allard, F., & Chabrier, G. 2015, *A&A*, 577, A42 [2.1](#), [2.3](#)
- Barnes, S. A. 2007, *ApJ*, 669, 1167 [1](#)
- Barrado y Navascués, D., Stauffer, J. R., & Jayawardhana, R. 2004, *ApJ*, 614, 386 [2.3](#), [10](#)
- Basri, G., Marcy, G. W., & Graham, J. R. 1996, *ApJ*, 458, 600 [1](#)
- Bastian, N., & de Mink, S. E. 2009, *MNRAS*, 398, L11 [1](#), [6](#)
- Bertelli, G., Nasi, E., Girardi, L., et al. 2003, *AJ*, 125, 770 [3.1.1](#)
- Boesgaard, A. M., Roper, B. W., & Lum, M. G. 2013, *ApJ*, 775, 58 [2.2](#), [10](#)
- Böhm, K.-H. 1963, *ApJ*, 138, 297 [3.1.1](#)
- Böhm-Vitense, E. 1958, *ZAp*, 46, 108 [5.3](#)
- Bonaca, A., Tanner, J. D., Basu, S., et al. 2012, *ApJ*, 755, L12 [5.3](#)
- Brandt, T. D., & Huang, C. X. 2015a, *ApJ*, 807, 58 [1](#), [3.1.1](#), [10](#), [5.1](#), [5.2](#), [6](#)
- . 2015b, *ApJ*, 807, 25 [1](#), [3.1.1](#)
- . 2015c, *ApJ*, 807, 24 [10](#), [5.1](#), [5.2](#)
- Brott, I., de Mink, S. E., Cantiello, M., et al. 2011, *A&A*, 530, A115 [1](#)
- Chaboyer, B., & Zahn, J.-P. 1992, *A&A*, 253, 173 [3.1.1](#)
- Choi, J., Conroy, C., & Byler, N. 2017, *ApJ*, 838, 159 [1](#)
- Choi, J., Dotter, A., Conroy, C., et al. 2016, *ApJ*, 823, 102 [1](#), [3.1](#), [3.1.1](#), [3.1.1](#), [5.2](#), [5.3](#), [6](#)
- Chun, S.-H., Yoon, S.-C., Jung, M.-K., Kim, D. U., & Kim, J. 2018, *ApJ*, 853, 79 [5.3](#)
- Conroy, C. 2013, *ARA&A*, 51, 393 [1](#)
- Correnti, M., Goudfrooij, P., Puzia, T. H., & de Mink, S. E. 2015, *MNRAS*, 450, 3054 [1](#)
- Cummings, J. D., Deliyannis, C. P., Maderak, R. M., & Steinhauer, A. 2017, *AJ*, 153, 128 [2.1](#), [2.2](#), [4.1](#), [10](#)
- Dahm, S. E. 2015, *ApJ*, 813, 108 [2.3](#), [10](#)
- de Bruijne, J. H. J., Hoogerwerf, R., & de Zeeuw, P. T. 2001, *A&A*, 367, 111 [2.1](#), [7](#), [12](#)

- de Jong, J. T. A., Rix, H.-W., Martin, N. F., et al. 2008, *AJ*, 135, 1361 [3.2](#)
- Dolphin, A. 1997, *New Astronomy*, 2, 397 [3.2](#), [3.3.1](#)
- Dolphin, A. E. 2002, *MNRAS*, 332, 91 [1](#), [3](#), [3.2](#), [3.3.1](#), [5.1](#)
- Dotter, A. 2016, *ApJS*, 222, 8 [1](#)
- Ekström, S., Georgy, C., Eggenberger, P., et al. 2012, *A&A*, 537, A146 [1](#), [3.1.1](#), [3.1.1](#), [5.2](#)
- Endal, A. S., & Sofia, S. 1978, *ApJ*, 220, 279 [3.1.1](#)
- Espinosa Lara, F., & Rieutord, M. 2011, *A&A*, 533, A43 [3.1.2](#), [3.2](#)
- Gaia Collaboration, Brown, A. G. A., Vallenari, A., et al. 2016, *A&A*, 595, A2 [1](#), [2.3](#)
- Gaia Collaboration, van Leeuwen, F., Vallenari, A., et al. 2017, *A&A*, 601, A19 [2.1](#), [1](#)
- Gallart, C., Zoccali, M., Bertelli, G., et al. 2003, *AJ*, 125, 742 [3.1.1](#)
- Gáspár, A., Rieke, G. H., Su, K. Y. L., et al. 2009, *ApJ*, 697, 1578 [1](#), [2.2](#)
- Gies, D. R., & Lambert, D. L. 1992, *ApJ*, 387, 673 [3.1.1](#), [5.2](#)
- Girardi, L., Bertelli, G., Bressan, A., et al. 2002, *A&A*, 391, 195 [1](#)
- Girardi, L., Bressan, A., Bertelli, G., & Chiosi, C. 2000, *A&AS*, 141, 371 [3.1.1](#)
- Girardi, L., Goudfrooij, P., Kalirai, J. S., et al. 2013, *MNRAS*, 431, 3501 [1](#)
- Goldman, B., Röser, S., Schilbach, E., et al. 2013, *A&A*, 559, A43 [2.1](#), [7](#)
- Goudfrooij, P., Girardi, L., & Correnti, M. 2017, *ApJ*, 846, 22 [6](#)
- Goudfrooij, P., Girardi, L., Kozhurina-Platais, V., et al. 2014, *ApJ*, 797, 35 [1](#)
- Gouliermis, D. A., Dolphin, A. E., Robberto, M., et al. 2011, *ApJ*, 738, 137 [3.2](#)
- Guenther, D. B., Demarque, P., Kim, Y.-C., & Pinsonneault, M. H. 1992, *ApJ*, 387, 372 [3.1.1](#)
- Gunn, J. E., Griffin, R. F., Griffin, R. E. M., & Zimmerman, B. A. 1988, *AJ*, 96, 198 [2.1](#)
- Heger, A., & Langer, N. 2000, *ApJ*, 544, 1016 [1](#)
- Heger, A., Langer, N., & Woosley, S. E. 2000, *ApJ*, 528, 368 [3.1.1](#), [5.2](#)
- Herrero, A. 1993, *Space Sci. Rev.*, 66, 137 [3.1.1](#)
- Huang, W., Gies, D. R., & McSwain, M. V. 2010, *ApJ*, 722, 605 [3.2](#), [5.2](#)
- Hunter, I., Brott, I., Langer, N., et al. 2009, *A&A*, 496, 841 [5.2](#)
- Jeffery, E. J., von Hippel, T., van Dyk, D. A., et al. 2016, *ApJ*, 828, 79 [1](#)
- Jørgensen, B. R., & Lindegren, L. 2005, *A&A*, 436, 127 [1](#)
- Joyce, M., & Chaboyer, B. 2018, *ApJ*, 856, 10 [5.3](#)
- Kalirai, J. S., & Tosi, M. 2004, *MNRAS*, 351, 649 [1](#)
- Katahira, J.-I., Hirata, R., Ito, M., et al. 1996, *PASJ*, 48, 317 [2.3](#)
- Kilian, J. 1992, *A&A*, 262, 171 [5.2](#)
- Kippenhahn, R., & Thomas, H.-C. 1970, in *IAU Colloq. 4: Stellar Rotation*, ed. A. Slettebak, 20 [3.1.1](#)
- Kopytova, T. G., Brandner, W., Tognelli, E., et al. 2016, *A&A*, 585, A7 [4.1](#)
- Kroupa, P. 2001, *MNRAS*, 322, 231 [3.2](#)
- Kurucz, R. L. 1970, *SAO Special Report*, 309 [3.1](#)
- . 1993, *SYNTHES spectrum synthesis programs and line data* [3.1](#)
- Levesque, E. M., Leitherer, C., Ekstrom, S., Meynet, G., & Schaerer, D. 2012, *ApJ*, 751, 67 [1](#)
- Li, T., Bedding, T. R., Huber, D., et al. 2018, *MNRAS*, 475, 981 [5.3](#)
- Lindegren, L., Madsen, S., & Dravins, D. 2000, *A&A*, 356, 1119 [2.3](#)
- Lucy, L. B. 1967, *ZAp*, 65, 89 [3.1.2](#)
- Madsen, S., Dravins, D., & Lindegren, L. 2002, *A&A*, 381, 446 [2.2](#), [2.3](#), [8](#), [9](#)
- Maeder, A. 1975, *A&A*, 43, 61 [3.1.1](#)
- . 1997, *A&A*, 321, 134 [1](#)
- . 1999, *A&A*, 347, 185 [1](#)
- Maeder, A., & Meynet, G. 2000a, *A&A*, 361, 159 [1](#), [3.1.1](#)
- . 2000b, *ARA&A*, 38, 143 [1](#)
- Maeder, A., & Zahn, J.-P. 1998, *A&A*, 334, 1000 [1](#), [5.2](#)
- Magic, Z., Serenelli, A., Weiss, A., & Chaboyer, B. 2010, *ApJ*, 718, 1378 [3.1.1](#)
- Magic, Z., Weiss, A., & Asplund, M. 2015, *A&A*, 573, A89 [5.3](#)
- Mamajek, E. E., & Hillenbrand, L. A. 2008, *ApJ*, 687, 1264 [1](#)
- Martín, E. L., Lodieu, N., Pavlenko, Y., & Béjar, V. J. S. 2018, *ArXiv e-prints*, arXiv:1802.07155 [2.1](#), [4.1](#), [10](#)
- Mazzei, P., & Pigatto, L. 1988, *A&A*, 193, 148 [1](#)
- McAlister, H. A., ten Brummelaar, T. A., Gies, D. R., et al. 2005, *ApJ*, 628, 439 [3.1.2](#)
- Mermilliod, J. C. 1981, *A&A*, 97, 235 [1](#)
- Meynet, G., & Maeder, A. 1997, *A&A*, 321, 465 [1](#)
- . 2000, *A&A*, 361, 101 [1](#)
- Meynet, G., Mermilliod, J.-C., & Maeder, A. 1993, *A&AS*, 98, 477 [1](#), [2.3](#), [10](#)
- Morel, T., Hubrig, S., & Briquet, M. 2008, *A&A*, 481, 453 [5.2](#)
- Mosumgaard, J. R., Silva Aguirre, V., Weiss, A., Christensen-Dalsgaard, J., & Trampedach, R. 2017, in *European Physical Journal Web of Conferences*, Vol. 160, European Physical Journal Web of Conferences, 03009 [5.3](#)
- Nelson, L. A., Rappaport, S., & Chiang, E. 1993, *ApJ*, 413, 364 [1](#)
- Nemravová, J., Harmanec, P., Kubát, J., et al. 2010, *A&A*, 516, A80 [2.3](#)
- Paxton, B., Bildsten, L., Dotter, A., et al. 2011, *ApJS*, 192, 3 [3.1](#), [3.1.1](#)
- Paxton, B., Cantiello, M., Arras, P., et al. 2013, *ApJS*, 208, 4 [3.1](#), [3.1.1](#)
- Paxton, B., Marchant, P., Schwab, J., et al. 2015, *ApJS*, 220, 15 [3.1](#), [3.1.1](#)
- Paxton, B., Schwab, J., Bauer, E. B., et al. 2018, *ApJS*, 234, 34 [3.1](#), [3.1.1](#), [3.1.1](#)
- Pearce, J. A., & Hill, G. 1971, *PASP*, 83, 493 [2.3](#)
- Penny, L. R. 1996, *ApJ*, 463, 737 [3.2](#)
- Perrin, M.-N., Cayrel de Strobel, G., Cayrel, R., & Hejlesen, P. M. 1977, *A&A*, 54, 779 [1](#)
- Perryman, M. A. C., Brown, A. G. A., Lebreton, Y., et al. 1997, *VizieR Online Data Catalog*, 333 [2.1](#)
- . 1998, *A&A*, 331, 81 [1](#), [2.1](#), [4.1](#), [10](#)
- Piatti, A. E., & Cole, A. 2017, *ArXiv e-prints*, arXiv:1705.08186 [1](#)
- Pinsonneault, M. H., Kawaler, S. D., Sofia, S., & Demarque, P. 1989, *ApJ*, 338, 424 [3.1.1](#)
- Ramírez-Agudelo, O. H., Simón-Díaz, S., Sana, H., et al. 2013, *A&A*, 560, A29 [3.2](#)
- Reino, S., de Bruijne, J., Zari, E., d'Antona, F., & Ventura, P. 2018, *MNRAS*, arXiv:1804.00759 [2.1](#)
- Richichi, A., Calamai, G., & Leinert, C. 1994, *A&A*, 286, 829 [2.3](#)
- Röser, S., Schilbach, E., Piskunov, A. E., Kharchenko, N. V., & Scholz, R.-D. 2011, *A&A*, 531, A92 [2.1](#)
- Royer, F., Zorec, J., & Gómez, A. E. 2007, *A&A*, 463, 671 [3.2](#)
- Salaris, M., & Cassisi, S. 2017, *Royal Society Open Science*, 4, 170192 [3.1.1](#)
- Shajn, G., & Struve, O. 1929, *MNRAS*, 89, 222 [1](#)
- Smart, W. M. 1939, *MNRAS*, 99, 168 [2.1](#)
- Soderblom, D. R., Laskar, T., Valenti, J. A., Stauffer, J. R., & Rebull, L. M. 2009, *AJ*, 138, 1292 [1](#), [2.3](#), [10](#)
- Stauffer, J. R., Hartmann, L. W., Fazio, G. G., et al. 2007, *ApJS*, 172, 663 [2.3](#), [9](#)
- Tayar, J., Somers, G., Pinsonneault, M. H., et al. 2017, *ApJ*, 840, 17 [5.3](#)
- Taylor, B. J. 2006, *AJ*, 132, 2453 [2.1](#), [1](#), [2.2](#)
- . 2008, *AJ*, 136, 1388 [1](#), [2.3](#)
- Taylor, B. J., & Jonek, M. D. 2005, *ApJS*, 159, 100 [2.1](#)
- Trampedach, R., Christensen-Dalsgaard, J., Asplund, M., Stein, R. F., & Nordlund, Å. 2015, in *European Physical Journal Web of Conferences*, Vol. 101, European Physical Journal Web of Conferences, 06064 [5.3](#)
- van Altena, W. F., Lee, J. T., & Hoffleit, E. D. 1997, *Baltic Astronomy*, 6, 27 [2.1](#)
- van Belle, G. T., Ciardi, D. R., ten Brummelaar, T., et al. 2006, *ApJ*, 637, 494 [3.1.2](#)
- VandenBerg, D. A., Richard, O., Michaud, G., & Richer, J. 2002, *ApJ*, 571, 487 [1](#)
- Viani, L. S., Basu, S., Ong, J. J. M., Bonaca, A., & Chaplin, W. J. 2018, *ArXiv e-prints*, arXiv:1803.05924 [5.3](#)
- von Zeipel, H. 1924, *MNRAS*, 84, 665 [1](#), [3.1.2](#)
- Vrancken, M., Lennon, D. J., Dufton, P. L., & Lambert, D. L. 2000, *A&A*, 358, 639 [3.1.1](#)
- Wang, P. F., Chen, W. P., Lin, C. C., et al. 2014, *ApJ*, 784, 57 [2.2](#), [8](#)
- Wayman, P. A. 1967, *PASP*, 79, 156 [2.1](#)

- Weisz, D. R., Dalcanton, J. J., Williams, B. F., et al. 2011, *ApJ*, 739, 5 [3.2](#)
- Woo, J.-H., Gallart, C., Demarque, P., Yi, S., & Zoccali, M. 2003, *AJ*, 125, 754 [3.1.1](#)
- Yen, S. X., Reffert, S., Schilbach, E., et al. 2018, *ArXiv e-prints*, arXiv:1802.04234 [1](#)
- Zhao, M., Monnier, J. D., Pedretti, E., et al. 2009, *ApJ*, 701, 209 [3.1.2](#)
- Zorec, J., & Royer, F. 2012, *A&A*, 537, A120 [3.2](#)
- Zwahlen, N., North, P., Debernardi, Y., et al. 2004, *A&A*, 425, L45 [2.3](#)

**Table 3**  
Best Fit Ages and [Fe/H]

Cluster	Filters	$\frac{\Omega}{\Omega_c}$	Age [Myr]	[Fe/H] <sup>1</sup>
The Hyades	$B_T, V_T$	0.0	$776^{+36}_{-15}$	$0.24^{+0.01}_{-0.03}$
		0.3	$676^{+13}_{-30}$	$0.24^{+0.02}_{-0.01}$
		$P(\frac{\Omega}{\Omega_c} = 0.3)$	$676^{+67}_{-11}$	$0.24 \pm 0.01$
	$J, K_s$	0.0	$741^{+17}_{-15}$	$0.10 \pm 0.01$
		0.6	$589^{+29}_{-11}$	$0.12 \pm 0.01$
		$P(\frac{\Omega}{\Omega_c} = 0.3)$	$741^{+55}_{-12}$	$0.10^{+0.01}_{-0.04}$
The Praesepe	$B_T, V_T$	0.0	$589^{+13}_{-14}$	$> 0.38$
		0.5	$589^{+13}_{-26}$	$0.24^{+0.03}_{-0.02}$
		$P(\frac{\Omega}{\Omega_c} = 0.3)$	$617^{+40}_{-10}$	$0.26^{+0.02}_{-0.04}$
	$J, K_s$	0.0	$741^{+42}_{-15}$	$0.08^{+0.01}_{-0.03}$
		0.4	$617^{+14}_{-13}$	$0.10 \pm 0.01$
		$P(\frac{\Omega}{\Omega_c} = 0.3)$	$617^{+17}_{-15}$	$0.09^{+0.01}_{-0.02}$
The Pleiades	$B_T, V_T$	0.0	$123^{+3}_{-15}$	$> 0.29$
		0.6	$141^{+27}_{-12}$	$> 0.40$
		$P(\frac{\Omega}{\Omega_c} = 0.3)$	$112^{+2}_{-26}$	$> 0.30$
	$J, K_s$	0.0	$162^{+182}_{-65}$	$> -0.01$
		0.6	$155^{+104}_{-37}$	$0.18^{+0.29}_{-0.15}$
		$P(\frac{\Omega}{\Omega_c} = 0.3)$	$155^{+150}_{-46}$	$> 0.03$

<sup>1</sup> Unbounded values are displayed as lower limits (e.g.,  $> 0.03$ ); see the beginning of §4.